

## RESEARCH ARTICLE

10.1002/2015JB012049

## Key Points:

- Afterslip on the Reelfoot fault can explain local, GNSS derived, crustal motion
- Lower crustal/upper mantle viscosity is greater than  $10^{21}$  Pa s
- Much of the present-day seismicity may be aftershocks of the 1811–1812 events

## Correspondence to:

O. S. Boyd,  
olboyd@usgs.gov

## Citation:

Boyd, O. S., R. Smalley Jr., and Y. Zeng (2015), Crustal deformation in the New Madrid seismic zone and the role of postseismic processes, *J. Geophys. Res. Solid Earth*, 120, 5782–5803, doi:10.1002/2015JB012049.

Received 19 MAR 2015

Accepted 8 JUL 2015

Accepted article online 14 JUL 2015

Published online 6 AUG 2015

## Crustal deformation in the New Madrid seismic zone and the role of postseismic processes

Oliver S. Boyd<sup>1</sup>, Robert Smalley Jr.<sup>2</sup>, and Yuehua Zeng<sup>1</sup>

<sup>1</sup>U.S. Geological Survey, Denver, Colorado, USA, <sup>2</sup>Center for Earthquake Research and Information, The University of Memphis, Memphis, Tennessee, USA

**Abstract** Global Navigation Satellite System data across the New Madrid seismic zone (NMSZ) in the central United States over the period from 2000 through 2014 are analyzed and modeled with several deformation mechanisms including the following: (1) creep on subsurface dislocations, (2) postseismic frictional afterslip and viscoelastic relaxation from the 1811–1812 and 1450 earthquakes in the NMSZ, and (3) regional strain. In agreement with previous studies, a dislocation creeping at about 4 mm/yr between 12 and 20 km depth along the downdip extension of the Reelfoot fault reproduces the observations well. We find that a dynamic model of postseismic frictional afterslip from the 1450 and February 1812 Reelfoot fault events can explain this creep. Kinematic and dynamic models involving the Cottonwood Grove fault provide minimal predictive power. This is likely due to the smaller size of the December 1811 event on the Cottonwood Grove fault and a distribution of stations better suited to constrain localized strain across the Reelfoot fault. Regional compressive strain across the NMSZ is found to be less than  $3 \times 10^{-9}$ /yr. If much of the present-day surface deformation results from afterslip, it is likely that many of the earthquakes we see today in the NMSZ are aftershocks from the 1811–1812 New Madrid earthquakes. Despite this conclusion, our results are consistent with observations and models of intraplate earthquake clustering. Given this and the recent paleoseismic history of the region, we suggest that seismic hazard is likely to remain significant.

### 1. Introduction

The New Madrid seismic zone in the central United States has been the host of several major earthquake sequences over the last several thousand years [Tuttle *et al.*, 2005, 2002] with three  $\sim$ M7+ earthquakes [Bakun and Hopper, 2004; Boyd and Cramer, 2014; Cramer and Boyd, 2014; Hough *et al.*, 2000; Hough and Page, 2011; Johnston, 1996] occurring over a 2 month period in the winter of 1811–1812. Whereas thrust events on the Reelfoot fault have been identified as the location for at least one of the large events in 1812 and 1450 [Carlson and Guccione, 2010], other large events are suggested to have occurred on the Cottonwood Grove fault, Bootheel lineament, and the New Madrid north fault [Hildenbrand and Hendricks, 1995; Johnston and Schweig, 1996; Mueller and Pujol, 2001], or outside the New Madrid seismic zone altogether [Hough *et al.*, 2005]. The magnitude and return period of these earthquakes have been at the center of scientific debate in recent years. Magnitudes from 6.8 to 8.4 and return periods from 160 to 10,000 or more years have been proposed. These factors have profound effects on estimates of seismic hazard and the potential loss of life. The latter, in turn, affects the costs associated with adopting acceptable levels of earthquake resistant construction and the extent of economic hardship associated with potential future New Madrid earthquakes.

The most recent papers to address the magnitudes of the 1811–1812 earthquakes are Boyd and Cramer [2014], Cramer and Boyd [2014], and Hough and Page [2011]. They reanalyze or reevaluate the reported intensities from the 1811–1812 earthquakes and estimate a range of magnitude between 7 and 7.7 for the three largest 1811–1812 events. Additional research addressing magnitudes of the 1811–1812 events based on seismic intensities has yielded ranges of 7.0–7.5 [Hough *et al.*, 2000], 7.5–7.8 [Bakun and Hopper, 2004], and 7.8–8.1  $\pm$  0.3 [Johnston, 1996].

Estimates of the return periods of New Madrid-type events have a similarly large variability. Tuttle *et al.* [2002] dated paleoliquefaction features in the New Madrid seismic zone (NMSZ) and discovered sequences of large earthquakes that occurred around  $900 \pm 100$  and  $1450 \pm 150$  AD. These older sequences are thought to be of similar magnitude to the earthquakes in 1811–1812 given a similar areal extent of liquefaction features [Tuttle *et al.*, 2002]. Based on these earthquakes and those in 1811–1812, Tuttle *et al.* [2002] infer an average return period of 500 years with a 95% confidence range of 160–1200 years.

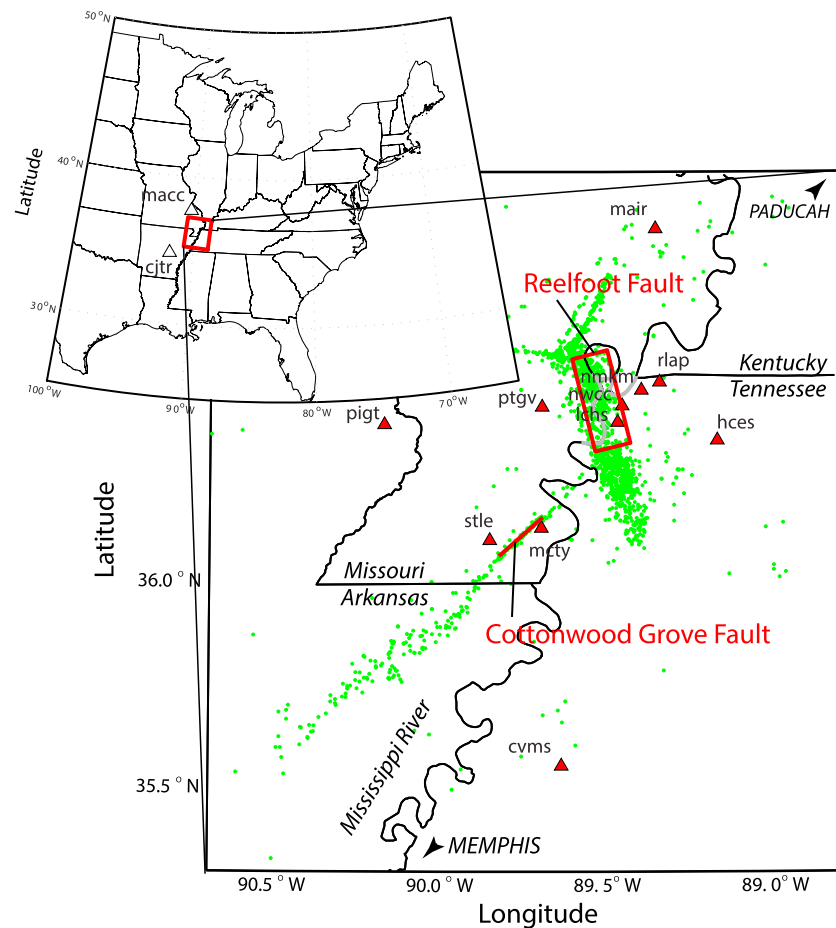


**Figure 1.** Stations from the Global Navigation Satellite System Array for Mid-America (GAMA) (triangles). The solid triangles are those that are used in the comparison to models of local creep and postseismic processes. Small circles are relocated epicenters of earthquakes measured in the region from 1995 to 2012.

More recently, several researchers have investigated geodetic motions using Global Navigation Satellite System (GNSS) data from the network of Continuously Operating Reference Stations (CORS; <http://geodesy.noaa.gov/CORS/>), which is a GNSS network of variable quality spread across the United States and primarily used for land surveying and navigation, and the GPS Array for Mid-America (GAMA; <http://www.ceri.memphis.edu/people/gps/index.html>), which is specifically designed for tectonic studies in and around the New Madrid seismic zone. *Calais and Stein* [2009] and *Craig and Calais* [2014] argue that relative motion across the NMSZ from far-field strain accumulation, as determined from GNSS sites distributed across the region, is less than 0.2 mm/yr, implying a return period of at least 10,000 years for M7 events with 2 m of average slip. *Frankel et al.* [2012] also analyzed the existing GNSS data in the region and found significant localized motion between several pairs of GAMA stations. They concluded that the motion could be explained by 4 mm/yr of creep on a 60 km long dislocation along the downdip extent of the Reelfoot fault at depths between 12 and 20 km. This motion, if steady over time, could lead to a M7.3 earthquake every 500 years.

In this study, we analyze GNSS data to confirm the presence of a creep signal and lack of regional strain and investigate several potential sources of the creep signal. Specifically, we analyze GNSS data from the GAMA network (Figure 1) and model the motion of these stations assuming a variety of kinematic and dynamic deformation processes including the following: (1) kinematically prescribed steady creep on subsurface dislocations residing along the downdip extensions of the Reelfoot and Cottonwood Grove faults, (2) dynamic models of viscoelastic relaxation and frictional afterslip from the 1811–1812 and 1450 New Madrid, MO, earthquakes, and (3) regional kinematically prescribed uniaxial compression and simple shear strain.

**Table 1.** Relative Velocities of the Stations in and Near the New Madrid Seismic Zone<sup>a</sup>

Station	Lat	Lon	Begin	End	Northing	Easting	Vertical
cvms	35.54	−89.64	2000.51	2013.12	0.02 ± 0.31	−0.03 ± 0.07	1.33 ± 1.08
cjtr	34.82	−92.27	2000.00	2014.94	0.60 ± 0.45	−0.19 ± 0.26	−0.08 ± 0.16
hces	36.33	−89.17	2003.12	2014.94	−0.11 ± 0.13	0.52 ± 1.12	−0.18 ± 0.95
lchs	36.38	−89.47	2008.03	2014.94	−0.10 ± 0.10	0.05 ± 0.16	−0.02 ± 0.21
macc	37.85	−90.48	2000.00	2014.94	−0.12 ± 0.22	−0.34 ± 0.05	−0.56 ± 0.83
mair	36.85	−89.36	2000.15	2014.94	0.02 ± 0.09	−0.05 ± 0.06	−0.08 ± 0.14
mcty	36.12	−89.70	2000.30	2013.84	−0.06 ± 0.17	−0.03 ± 0.08	0.21 ± 0.69
nmkm	36.45	−89.40	2008.03	2014.94	0.11 ± 0.20	−0.08 ± 0.17	−0.21 ± 0.36
nwcc	36.42	−89.46	2000.53	2014.91	0.11 ± 0.25	0.03 ± 0.44	1.00 ± 0.47
pigt	36.37	−90.18	2002.01	2014.94	−0.09 ± 0.45	0.26 ± 0.12	−1.32 ± 1.13
ptgv	36.41	−89.70	2000.00	2014.94	−0.04 ± 0.04	−0.07 ± 0.10	−0.31 ± 0.15
rlap	36.47	−89.35	2009.65	2014.94	0.16 ± 0.44	−0.32 ± 0.44	0.10 ± 0.51
stle	36.09	−89.86	2000.32	2014.94	0.10 ± 0.04	0.06 ± 0.07	0.06 ± 0.14

<sup>a</sup>Northing, easting, and vertical motions are expressed in mm/yr. Uncertainties are one standard error.

Multiple studies have explored some of these dynamic models. *Li et al.* [2005] performed viscoelastic finite element modeling to estimate the stress evolution in the New Madrid region following the 1811–1812 earthquakes in order to appreciate the potential for earthquakes in the surrounding region. *Kenner and Segall* [2000] performed viscoelastic modeling to show that viscoelastic relaxation can reload the seismogenic upper crust leading to a cluster of earthquakes with return periods shorter than the long-term average.

## 2. GNSS Data Analysis

GNSS time series are prepared through a series of steps to identify and remove poor quality data and offsets, and estimate and remove nontectonic periodic signals. The steps of removing offsets and estimating and removing nontectonic periodic signals are repeated in order to account for the effect of periodic signals in estimating the offsets. The relative motion between an individual station and a stack of a subset of the stations used to define a reference frame, as described in the next section, is then calculated and used for modeling. While estimating motion relative to a reference frame is equivalent to removing a rigid body rotation, which also occurs during modeling inversion, motion relative to this local reference frame yields a more representative estimate of the uncertainty of station velocities by removing time-varying signals common to all stations.

Time series for the northerly, easterly, and vertical components of motion relative to North America in the ITRF2008 reference frame [*Altamimi et al.*, 2011] for 13 GNSS stations residing within the GAMA network were obtained from the website <http://earthquake.usgs.gov/monitoring/gps/data/networks/CentralUS/> in December 2014 and span the time period from mid-1999 to late 2014 (Table 1). These time series were processed by the USGS with the GNSS processing software GYPSY [*Bertiger et al.*, 2010; *Zumberge et al.*, 1997].

The original time series have strong seasonal components, offsets, gaps, and periods during which equipment failure produced bad data or the data appear anomalous (Figure 2). For example, station *rlap* had a bad antenna from January 2006 until August 2009 resulting in anomalous excursions of the GNSS data. The antenna was replaced in August of 2009. Station *pigt* also had equipment problems at least before 2001 when its receiver was only tracking satellites above some very large mask angle (somewhere between 30° and 45°). Further, the easterly component of station *pigt* has an unusually strong seasonal signal and several large offsets due to equipment changes. Similar to *pigt*, the northerly and easterly components of station *hces* are particularly noisy.

The first step in preparing the data is to remove sections of known bad data due to equipment problems and then to identify sections of poor data quality. A total of 15 sections were identified and removed from the 39 time series and are listed in Table 2. Additional data are removed if an offset is likely to have occurred within an existing gap or extended region of bad data. Removal of the additional data is done because the offset cannot be estimated with precision when residing within a large data gap. Therefore, all of the data either prior to or after the offset are discarded, depending on the length and quality of the remaining time series segments where preference is given to the longer more continuous segment.

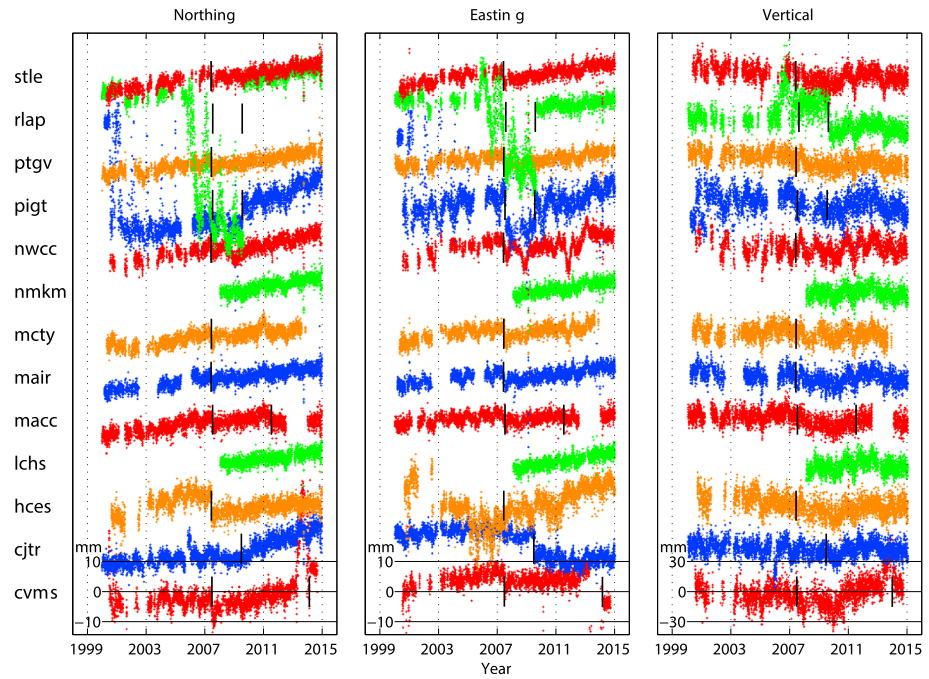


**Figure 2.** Original time series from the stations in Figure 1 relative to a regional reference frame. The vertical components are reduced in amplitude by a factor of three relative to the northing and easting. Thick vertical lines denote the locations of interpreted offsets (Table 3).

For example, bad data due to equipment problems are observed at *rlap* from about 2006 to 2009. At the beginning of this period, the radome was replaced, and at the end, the antenna was replaced. Because these equipment changes could have caused offsets in the data and the intervening time series was removed, we choose to remove all data before 2009. For this particular case, we could have created a new time series for the data prior to 2006, but there are several gaps and two potential offsets that reduce our confidence in these data.

The next step in the process is to remove offsets. We assume that potential offsets coincide with replacement of the radome or antenna at the GNSS station (bold entries in Table 3). Times at which the receiver was replaced, the receiver firmware updated (not listed in Table 3), or the antenna’s low noise amplifier replaced do not appear to cause offsets in these time series. We remove an additional offset on 23 July 2009 for station *pigt*, but the cause of the offset is unknown. We take 182 days of GNSS positions on either side of the offset and perform a grid search to find the offset that minimizes the variance of the detrended time series.

**Table 2.** Sections, by Year and Decimal Date, of the Time Series Removed From the Analysis<sup>a</sup>

Station	Component	Begin	End
<i>cvms</i> <sup>b</sup>	N,E,V	2013.12	2016.00
<i>cjtr</i> <sup>c</sup>	N,E,V	2005.70	2006.03
<i>hces</i> <sup>d</sup>	N,E,V	1999.00	2003.00
<i>pigt</i> <sup>e</sup>	N,E,V	1999.00	2002.00
<i>rlap</i> <sup>f</sup>	N,E,V	1999.00	2009.65

<sup>a</sup>Each section is removed from all three components resulting in 15 sections removed from the 39 time series.

<sup>b</sup>Data removed due to large gap around offset.

<sup>c</sup>Data removed due to it being anomalously noisy.

<sup>d</sup>Data removed due to it being anomalously noisy.

<sup>e</sup>Data removed due to bad receiver.

<sup>f</sup>Data removed due to bad data and resulting gap around offsets.

Next, periodic signals present within the time series are estimated and removed using a method similar to that described by *Roeloffs* [2001]. For each time series represented with serial dates and each day, *d*, in 1 year having a period of 365.24 days, all sample positions within 30 days of *d* for each available cycle are averaged. The resulting periodic signals are shown in Figure 3 and subtracted from the time series in Figure 2.

The primary periodic signals are annual and semi-annual signals. However, we

**Table 3.** Equipment Changes and Offsets Identified and Removed From the Time Series<sup>a</sup>

Station	Equipment Change	Month	Day	Year
cvms	Receiver	7	16	2003
cvms	Receiver	3	2	2007
<b>cvms</b>	<b>Antenna</b>	<b>6</b>	<b>26</b>	<b>2007</b>
cvms	Receiver	5	17	2010
cvms	Receiver	8	3	2012
<b>cvms</b>	<b>Radome</b>	<b>2</b>	<b>25</b>	<b>2014</b>
cjtr	Receiver	3	14	2007
<b>cjtr</b>	<b>Radome</b>	<b>12</b>	<b>10</b>	<b>2007</b>
hces	Receiver	2	4	2005
<b>hces</b>	<b>Radome</b>	<b>7</b>	<b>7</b>	<b>2005</b>
<b>hces</b>	<b>Radome</b>	<b>6</b>	<b>11</b>	<b>2007</b>
hces	Receiver	2	16	2012
hces	Receiver	4	11	2012
lchs	Receiver	2	16	2012
macc	Receiver	3	30	2005
<b>macc</b>	<b>Radome</b>	<b>7</b>	<b>13</b>	<b>2007</b>
<b>macc</b>	<b>Antenna</b>	<b>7</b>	<b>15</b>	<b>2011</b>
macc	Low noise amplifier	9	5	2012
mair	Receiver	2	10	2006
mair	Receiver	9	9	2006
<b>mair</b>	<b>Radome</b>	<b>6</b>	<b>4</b>	<b>2007</b>
mair	Receiver	9	4	2012
mcty	Receiver	2	3	2005
<b>mcty</b>	<b>Radome</b>	<b>6</b>	<b>12</b>	<b>2007</b>
mcty	Receiver	3	3	2011
mcty	Receiver	10	25	2013
nwcc	Receiver	3	7	2007
<b>nwcc</b>	<b>Radome</b>	<b>6</b>	<b>5</b>	<b>2007</b>
pigt	Receiver	2	24	2006
pigt	Receiver	12	1	2006
<b>pigt</b>	<b>Radome</b>	<b>7</b>	<b>13</b>	<b>2007</b>
<b>pigt</b>	<b>Unknown</b>	<b>7</b>	<b>23</b>	<b>2009</b>
pigt	Receiver	11	29	2012
ptgv	Receiver	12	20	2004
<b>ptgv</b>	<b>Radome</b>	<b>6</b>	<b>12</b>	<b>2007</b>
rlap	Receiver	5	17	2005
<b>rlap</b>	<b>Radome</b>	<b>6</b>	<b>5</b>	<b>2007</b>
<b>rlap</b>	<b>Antenna</b>	<b>8</b>	<b>10</b>	<b>2009</b>
stle	Receiver	9	10	2006
<b>stle</b>	<b>Radome</b>	<b>6</b>	<b>5</b>	<b>2007</b>
stle	Receiver	9	4	2012

<sup>a</sup>Items in bold are equipment changes (radomes and antennas) seen to cause offsets in the time series.

averaged. This process is equivalent to removing a common mode, as is employed by other investigators [Wdowinski *et al.*, 1997]. It is interesting to note that the reference time series is moving northeast relative to the ITRF2008 North American reference frame and may be due to glacial isostatic adjustment [Calais *et al.*, 2006].

The slope of the differential time series (i.e., the velocity of the station relative to the reference) is found using an iteratively reweighted least squares method with the Robustfit function in Matlab version R2014a with default values, which uses the bisquare penalty function thereby ignoring gross outliers. The resulting velocities for the GNSS stations in and around the NMSZ are presented in Table 1. A subset of the velocity vectors appears in Figure 5. These values are used in the deformation modeling presented in section 5.

We find that relative motion is likely occurring between stations of the GAMA network (Figure 5) as is also shown by Frankel *et al.* [2012]. They found significant motions between several pairs of sites. For example, between stations *stle* and *ptgv*, *mair*, and *macc*, they found that the pairs of sites are moving toward each

find that these signals are modulated by signals with periods of about 5 and 12 years, which may be caused by North American meteorological anomalies related to the Pacific and Atlantic Ocean decadal oscillations, which are in turn affected by the Southern Oscillation in the tropical Pacific Ocean [Cane and Zebiak, 1985; Enfield *et al.*, 2001; Gershunov and Barnett, 1998; Mo, 2010]. While other GNSS studies are beginning to see these signals [Silverii *et al.*, 2014], additional research is required to understand this potential connection. At this time, we choose not to estimate and remove the super-annual signals because estimating the signal for a given time series is uncertain and could potentially introduce velocity artifacts. We note, however, that leaving these signals in the time series will increase our estimate of the velocity uncertainty.

### 3. Relative Motion Between GNSS Sites

The relative motion between GNSS sites is found by examining the difference between a station's time series and a reference time series. The reference time series (bottom trace in Figure 4) is found by stacking the time series from all GAMA stations except *cjtr*, *hces*, and *pigt*. Station *cjtr* is relatively far from the NMSZ, and *pigt* and *hces* are relatively noisy. For some days, not all of the stations have data. In this case, data for the available stations are

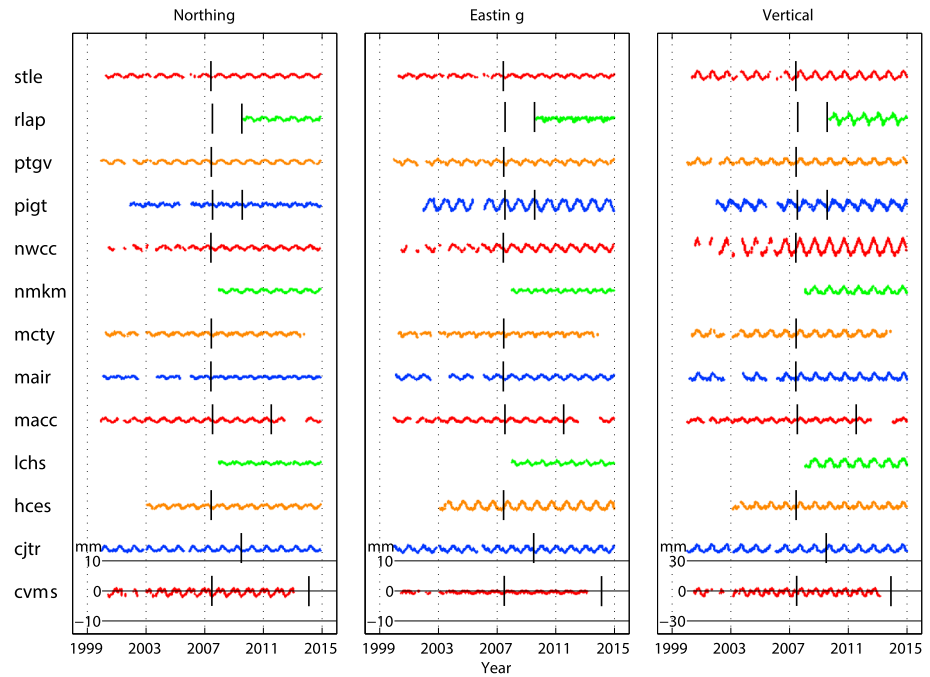


Figure 3. Periodic signals determined for the stations in Figure 1.

other at a rate and one standard error of  $0.37 \pm 0.07$ ,  $0.23 \pm 0.03$ , and  $0.37 \pm 0.12$  mm/yr in the east-west direction and  $0.12 \pm 0.07$ ,  $0.15 \pm 0.12$ , and  $0.12 \pm 0.07$  mm/yr in the north-south direction, respectively. In this analysis, we find that these sites are also moving toward each other at a rate of  $0.13 \pm 0.08$ ,  $0.11 \pm 0.06$ , and  $0.39 \pm 0.06$  mm/yr in the east-west direction and  $0.14 \pm 0.04$ ,  $0.08 \pm 0.06$ , and  $0.23 \pm 0.13$  mm/yr in the north-south direction, respectively, where the uncertainties—discussed in the next section—are one standard error and the average of the two components, which assumes some correlation between the pairs of time series.

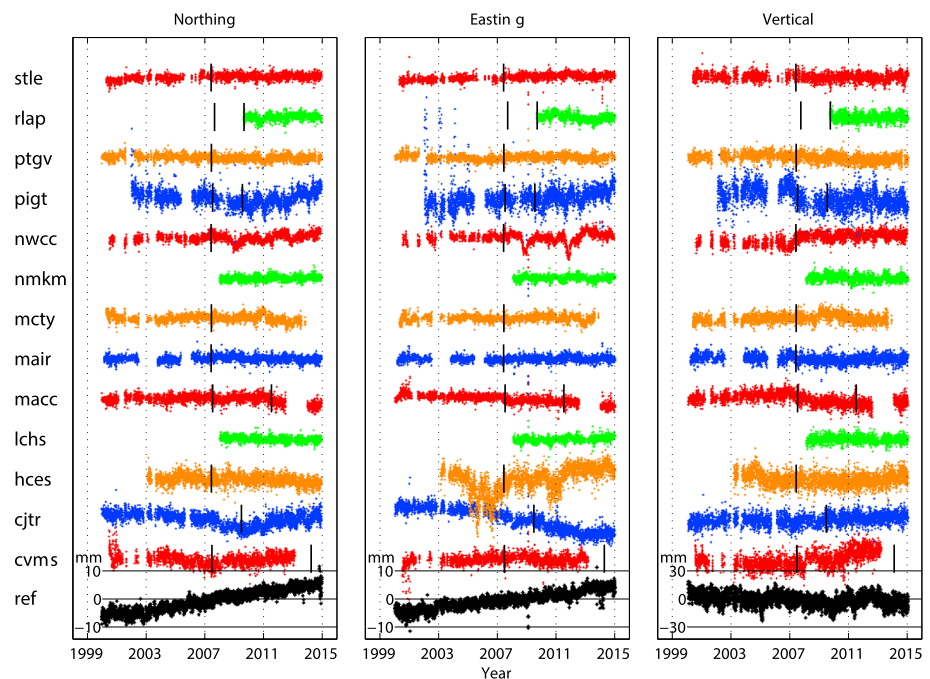
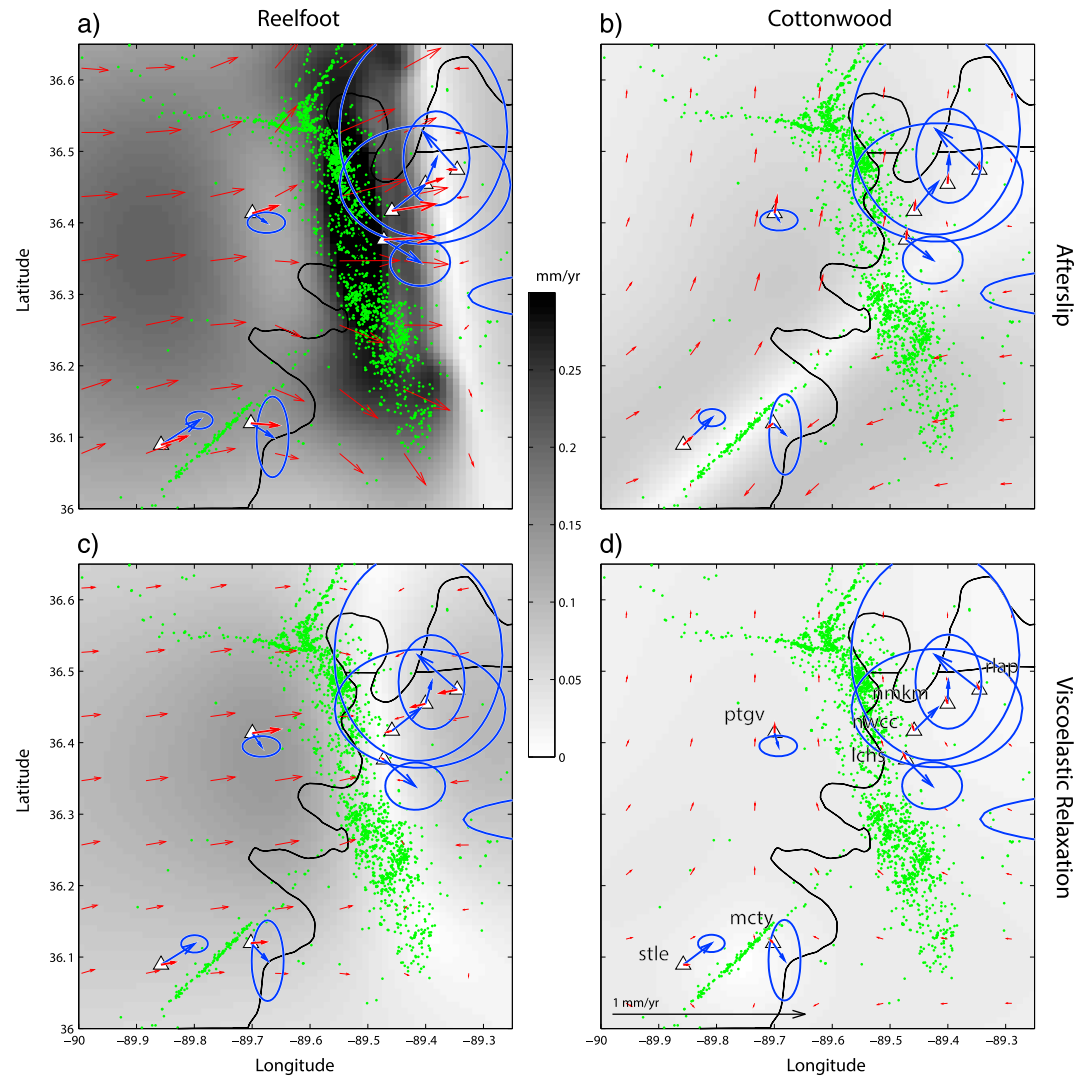


Figure 4. Cleaned differential times series. Poor quality data (Table 2), offsets (Table 3), and periodic sinusoids are removed. The bottom series labeled “ref” is a stack of the cleaned time series indicated by horizontal lines.



**Figure 5.** Surface deformation resulting from (a and b) afterslip and (c and d) viscoelastic models for 5 m of slip in the Reelfoot fault earthquakes and 3.75 m in the Cottonwood Grove fault earthquakes. Vectors with ellipses are the observed station velocities and their one-sigma uncertainty. A local reference frame, solved for with northing and easting translations and explained in the text, has been removed. Gray shading and arrows without ellipses are the magnitude and vectors, respectively, of horizontal surface velocities resulting from postseismic models from earthquakes on the (a and c) Reelfoot and (b and d) Cottonwood Grove faults. Dots are relocated seismicity.

#### 4. Estimates of Uncertainty

Uncertainty in GNSS time series is commonly considered to be due to a combination of three noise sources [Mao *et al.*, 1999]. These sources are white, flicker, and random walk. White noise has a frequency-independent power spectrum and, for long time series, generally contributes little to velocity uncertainty. Flicker and random walk noise sources have increasing power with decreasing frequency, which increases their contribution to the velocity uncertainty [Williams, 2003]. Random walk is the most difficult to assess—due to the relatively short duration of the time series and the amount of white and flicker noise present—and in most cases is the greatest contribution to uncertainties of velocity estimates. In the frequency domain, the three noise sources have a frequency dependence of  $1/f^0$ ,  $1/f^1$ , and  $1/f^2$ , respectively. The uncertainty in each GNSS time series is determined by estimating the contribution of these three noise sources and then simulating 500 time series containing this noise and the gaps present in the real data. Velocities are determined for each simulated time series using the procedure outlined in the previous section, and the standard deviation of these velocities is the velocity uncertainty for the GNSS time series.

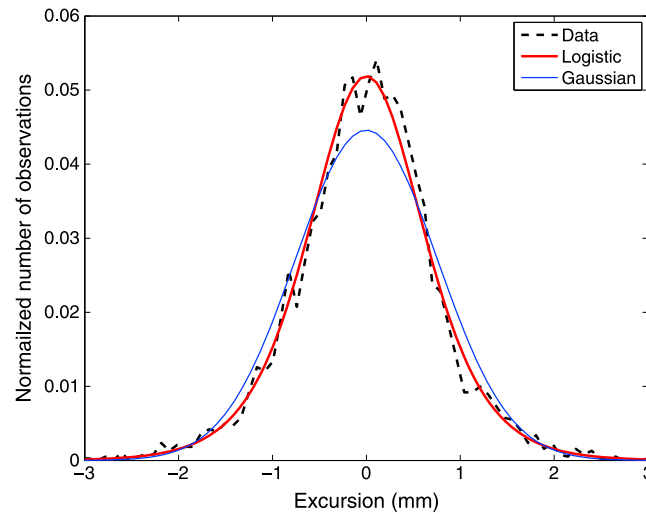


**Figure 6.** Distribution of daily positions for station *stle* after removing a linear trend and low frequency signal. The dashed curve is the observed distribution, and the solid thick and thin curves are logistic and Gaussian fits, respectively. The fit for the logistic distribution is found with a grid search and minimizing the summed absolute difference between observed and predicted values. The Gaussian fit is found by using the standard deviation of the observations. Both distributions have an area of 1 beneath the curves. If instead the Gaussian fit was found by matching the height of the observed data, which is accomplished by reducing the Gaussian fit's standard deviation, the fitted distribution would fall even farther below the observed tails.

signal, has a strong peak with relatively broad tails, a combination better suited to the logistic distribution. The low frequency signal is estimated using the Matlab function `gridfit`, which uses a modified ridge estimator [Swindel, 1976] to generate a smooth surface. Our observation of the underlying distribution of the white noise component is not an artifact of the presence of and our process of removing flicker and random walk noise sources, which we confirm with synthetic time series. For a given standard deviation of GNSS motions, Gaussian and logistic distributions yield the same velocity uncertainty. However, if robust methods are employed to estimate the slope of the position time series, e.g., an iteratively reweighted least squares method, assuming an underlying Gaussian distribution will yield an overestimate of the rate uncertainty due to the white noise component.

A weighted least squares inversion is used to solve equation (1) for the three components of noise. The weights are equal to frequency in order to compensate to some extent for the interpolation to log space when calculating smooth spectra. This method is tested on simulated series with the characteristics of our observed time series to ensure that we are able to recover, on average, the components of the three noise sources. The contributions of the noise sources are reported in Table 4 in terms of noise amplitude [Williams, 2003],  $\sigma_w$ ,  $\sigma_{FL}$ , and  $\sigma_{RW}$ :

$$\sigma_k = \sqrt{\frac{s_k f_s^{k/2}}{2(2\pi)^k}} \quad (2)$$

Here  $k$  is the frequency dependence of the noise source, equal to 0 for white noise, 1 for flicker, and 2 for random walk,  $s_k$  is the power spectral amplitude of the  $k$ th noise source, and  $f_s$  is the sampling frequency equal to 365.24 samples per year. Figure 7 shows observed and simulated spectra and time series for the east component of station *stle*. Even though random walk contributes less to the spectrum over the frequencies analyzed, it contributes most to velocity uncertainty, about 70%, whereas flicker contributes about 28% and white noise, 2%.

The white noise component for the GNSS stations in this analysis has values of the white noise amplitude,  $\sigma_w$ , ranging from 0.5 to 5.8 mm (neglecting station *nwcc*, which has variability in the time series that cannot be

The power spectrum composed of these three noise sources is

$$S(f) = s_w + \frac{s_{FL}}{f} + \frac{s_{RW}}{f^2}, \quad (1)$$

where  $S(f)$  is the observed spectrum,  $s_w$  is the white noise component,  $s_{FL}$  is the flicker component, and  $s_{RW}$  is the random walk component. This model is compared with a spectral estimate of the 5% cosine tapered detrended differential GNSS time series. The spectral estimates are calculated using a multitaper spectral method [Thomson, 1982], smoothed, and then interpolated in log frequency space.

Previous analyses of white noise in GNSS time series have typically assumed a Gaussian distribution [Mao et al., 1999; Zhang et al., 1997], but here the distribution of relative GNSS positions for every component of every station is better represented by a logistic distribution, as shown in Figure 6 for one component of station *stle*. The distribution of GNSS data, after removal of a linear trend and low frequency

**Table 4.** Contributions to Noise<sup>a</sup>

Station	Northing			Easting			Vertical		
	$\sigma_W$	$\sigma_{FL}$	$\sigma_{RW}$	$\sigma_W$	$\sigma_{FL}$	$\sigma_{RW}$	$\sigma_W$	$\sigma_{FL}$	$\sigma_{RW}$
cvms	0.97	3.0	1.012	0.93	2.7		4.66	11.4	3.353
cjtr	1.21	2.5	1.615	0.98	2.4	0.942	4.13	7.6	
hces	1.15	2.5	0.341	1.67	6.9	3.458	5.24	8.9	2.987
lchs	0.68	0.9	0.202	0.61	1.6	0.347	3.02	4.2	
macc	0.82	2.0	0.758	0.74	1.2	0.146	3.23	7.1	3.012
mair	0.71	1.4	0.305	0.69	1.2	0.179	2.93	6.2	
mcty	0.51	2.5	0.520	0.54	2.0	0.233	2.88	6.1	2.321
nmkm	0.70	0.9	0.464	0.50	1.8	0.344	2.11	6.9	
nwcc	0.54	2.5	0.861	0.00	4.1	1.449	2.76	8.4	1.454
pigt	1.36	4.3	1.425	2.18	4.7		5.77	17.3	3.489
ptgv	0.73	1.4	0.107	0.67	1.3	0.356	2.93	6.4	
rlap	0.81	1.2	0.901	0.61	2.3	0.905	2.99	7.0	
stle	0.66	1.5		0.60	1.1	0.230	2.77	6.0	
ref	0.75	2.5		0.61	2.8		2.65	13.7	

<sup>a</sup>Contributions are from white ( $\sigma_W$ ), flicker ( $\sigma_{FL}$ ) and random walk ( $\sigma_{RW}$ ) noise source models for each component of each station. Units are mm for white noise,  $\text{mm/yr}^{1/4}$  for flicker, and  $\text{mm/yr}^{1/2}$  for random walk. For cells without values, random walk was not estimated, because it was too small relative to the amount of white and flicker noise present in the time series.

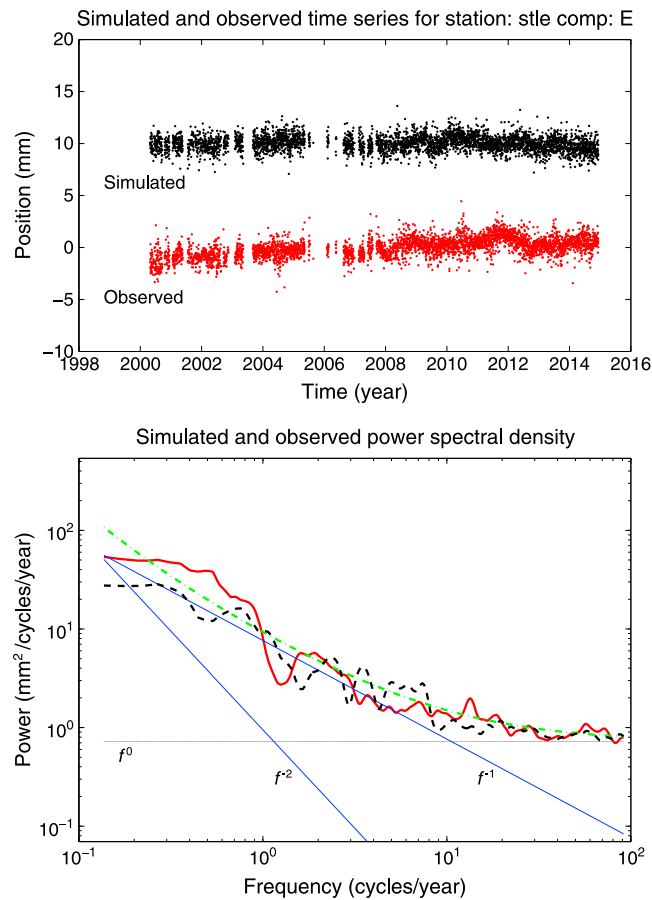


**Figure 7.** Example of the uncertainty analysis for the east component of station *stle*. The upper figure shows (bottom) the processed observed series and (top) a simulated series. The lower figure shows the observed series spectra (solid thick curve), simulated spectra (dashed curve), and fitted spectra (dash-dotted curve). Also shown in this subplot are the three noise sources (straight lines of varying slope) that contribute to the fitted spectra.

well fit with the noise model we have chosen) with the vertical contribution being about three to five times greater than the horizontals. Stations *pigt* and *hces* generally have the largest amounts of white noise, which are about a factor of two greater than the other stations.

The flicker noise component has noise amplitudes,  $\sigma_{FL}$ , ranging from 0.9 to 17  $\text{mm/yr}^{1/4}$ . The vertical contribution tends to be about a factor of three to four greater than the horizontals. Again, stations *pigt* and *hces* have relatively large values with *pigt* about a factor of two to four greater than the other stations.

The random walk noise component contributes most to the uncertainty in velocity estimates and is also the most difficult to estimate because of the amount of white and flicker noise and the relatively short time series. For those stations where the inversion yielded a value greater than zero, the noise amplitude,  $\sigma_{RW}$ , ranges from 0.1 to 3.5  $\text{mm/yr}^{1/2}$ . In most cases, the vertical amount of random walk noise is greater than the horizontals.

The estimated velocity uncertainties for each component of each station are given in Table 1 and shown for a subset of the stations with ellipses in Figure 5.

The uncertainties are very similar to maximum likelihood estimates of uncertainty reported by the program `est_noise` [Langbein, 2004]. Uncertainties range from 0.04 mm/yr to 1.1 mm/yr and average about 0.33 mm/yr. Vertical uncertainties are about a factor of two greater than the horizontals. The horizontal uncertainties are critical to the modeling analysis, as will become clear in the next section, and are themselves uncertain. Implementing the spectral fitting described above on simulated series with specified amounts of these three noise sources will result in a range of white, flicker, and random walk estimates with the greatest range for random walk. For instance, the uncertainty for the easting component of station *stle* is uncertain by a factor of 2, though, because of the distinct character of each noise source, the distribution of possible uncertainties is not exactly lognormal. Other sources of velocity uncertainty and potential bias that are not considered are due to the following: (1) uncertainties when removing offsets, (2) the effect of offsets on the estimates of the other noise sources, (3) uncertainties in the removal of the periodic signals, and (4) the potential contribution from super-annual signals.

## 5. Modeling the GNSS Velocities

The differential GNSS velocity vectors are compared to a series of individual kinematic and dynamic models of physical processes that may be active in the New Madrid region. Our list of candidate models, detailed in the next paragraph, is not exhaustive or mutually exclusive. Many more possible sources of ground deformation could be present in the region, including glacial isostatic adjustment [Sella *et al.*, 2007], traction at the base of the lithosphere focused beneath the central United States [Forte *et al.*, 2007], lithospheric adjustment subsequent to erosion in the upper Mississippi embayment [Calais *et al.*, 2010], and density anomalies within the mid to lower crust [Pollitz *et al.*, 2001]. Additional work and data will be required to tease out the contribution from all potential sources of ground deformation in the New Madrid region.

The processes modeled here include the following: (1) kinematically prescribed steady creep on dislocations residing along the downdip extensions of the Reelfoot fault [Frankel *et al.*, 2012] and Cottonwood Grove fault; (2) dynamic models of postseismic viscoelastic relaxation and frictional afterslip from the 16 December 1811 earthquake on the Cottonwood Grove fault, the 17 February 1812 earthquake on the Reelfoot fault [Kenner and Segall, 2000; Li *et al.*, 2005], and two of the ~1450 AD earthquakes on the Cottonwood Grove and Reelfoot faults; and (3) kinematically prescribed large scale uniaxial compression and simple shearing of the region [Pratt, 2012]. Note that postseismic afterslip is one explanation for creep. These two models are not necessarily different.

Postseismic processes from the 23 January 1812 event and creep on a deep extension of the causative fault are not modeled because it appears to be the smallest of the three 1811–1812 events, and its location is not as well known and may lie to the north where geodetic instrumentation is sparse [Cramer and Boyd, 2014; Hough *et al.*, 2005]. The region around the 16 December event also suffers from a lack of dense geodetic instrumentation and some ambiguity in its location. Possible structures that may have hosted this event are the Cottonwood Grove fault or the Bootheel lineament [Johnston and Schweig, 1996]. The Cottonwood Grove fault is chosen because present-day seismicity is concentrated along this trend (Figure 1). Whereas the February 1812 event and at least one of the 1450 events are observed to have occurred on the Reelfoot fault [Carlson and Guccione, 2010], the location of the southern NMSZ 1450 event is uncertain. We assume it occurred on the Cottonwood Grove fault but acknowledge that this may not have been the host fault. The 900 AD and older earthquakes are not modeled because their contribution to present-day ground deformation is expected to be smaller than the 1811–1812 and 1450 AD earthquakes, and their locations are not well known.

### 5.1. Fault Geometry, Extent of Rupture, and Slip in the 1811–1812 and 1450 Events

Planes are fit to relocated seismicity [DeShon *et al.*, 2011; Dunn *et al.*, 2013] to estimate strike, dip, and position of the Reelfoot and Cottonwood Grove faults (Table 5 and Figure 1). North of the intersection of the Cottonwood Grove and Reelfoot faults between about 5 and 10 km depth, the Reelfoot fault dips at about 32 degrees to the west and strikes N7W. South of this intersection, seismicity resides on several trends of varying orientation; consequently, we restrict February 1812 coseismic rupture to the north of this intersection. Over the same depth range, the Cottonwood Grove fault is nearly vertical and strikes N48E. With regard to the shallow extent of the Reelfoot fault, Van Arsdale *et al.* [1998] used seismic reflection data to find that the Reelfoot fault dips at 73 degrees to the west just below the Reelfoot scarp. Given the dip and outcropping

**Table 5.** Parameters of the Faults Considered in This Study<sup>a</sup>

Structure	Slip	Strike	Dip	Rake	Length	Top	Bottom	Lat.	Lon.
<i>Coseismic Fault Parameters</i>									
Cottonwood Grove fault	3.75	47.6	86.2	0	20	2	10	36.098	-89.767
Reelfoot fault, seg. A	6.63	173.2	73.0	90	40	0	5.1	36.401	-89.450
Reelfoot fault, seg. B	5.00	173.2	31.9	90	40	5.1	10	36.410	-89.359
<i>Afterslip</i>									
Cottonwood Grove fault	47.6	86.2	0	100	10	50	36.098	-89.767	
Reelfoot fault	173.2	31.9	90	200	10	100	36.410	-89.359	
<i>Creeping Dislocations</i>									
Cottonwood Grove fault	47.6	86.2	0	20	12	20	36.098	-89.767	
Reelfoot fault	173.2	31.9	90	40	12	20	36.410	-89.359	
Regional shear	28.0	90.0	0	2000	20	1000	36.300	-89.600	

<sup>a</sup>Slip is in meters. Strike is degrees clockwise relative to north, dip is perpendicular to strike in the clockwise direction and down from the horizontal, and rake is relative to horizontal, 90 being thrust and 0 being right-lateral strike slip. Length, top, and bottom are in kilometers. Latitude (Lat.) and longitude (Lon.) refer to the location of the middle of the surface projection of the structure.

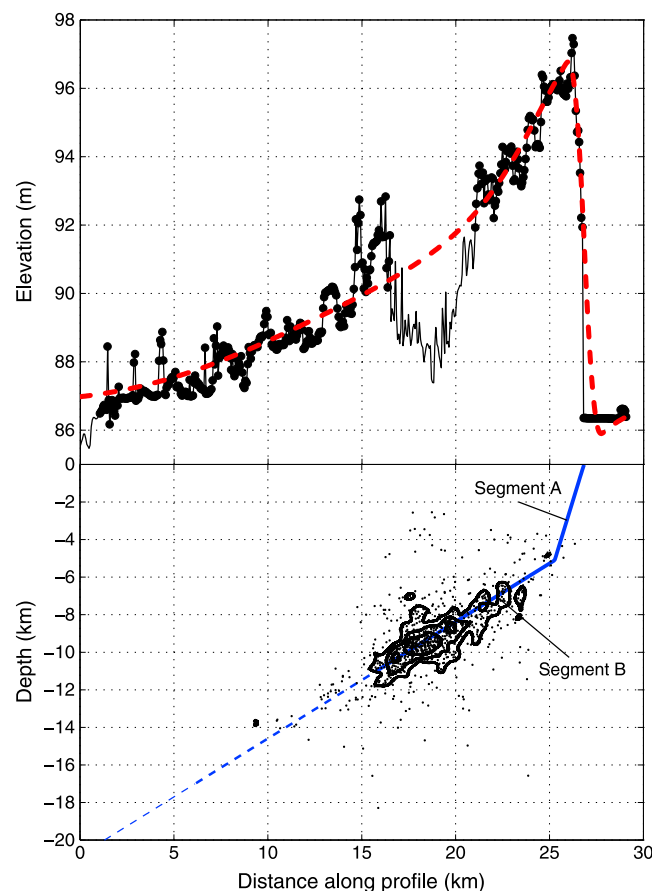


**Figure 8.** (Upper plot) Measured (large dots and thin line) and modeled (dashed line) surface topography and (lower plot) subsurface Reelfoot faults, segments A and B, as viewed along the strike of the Reelfoot fault. Dashed lines along the subsurface faults are the extent of the fault participating in afterslip. Present-day topography is best modeled by uniform slip (coseismic and postseismic) extending from the surface to 17 km depth. Dots in the bottom panel are earthquakes along the Reelfoot fault. Contours show 10%, 25%, and 50% of the maximum spatial density.

position of the upper segment of the Reelfoot fault, segment A, and the position and orientation of the lower segment, segment B, these fault segments should meet in the subsurface at about 5 km depth (Figure 8).

Present-day topography can provide a constraint on the total amount and extent of coseismic and postseismic slip that has occurred on the Reelfoot fault since the 1450 AD event [Carlson and Guccione, 2010]. In Figure 8, topographic highs from a USGS 90 meter digital elevation model [Gesch et al., 2002] along a transect perpendicular to the strike of the Reelfoot fault from about 89.39°W, 36.31°N to 89.42°W, 36.51°N are displayed. Highs are considered in this particular analysis, because alluvial processes have extensively dissected much of the region. As a result of these surficial processes, means and medians are less likely to reflect the underlying structural relief.

Total amount and extent of slip are determined by minimizing the difference between observed and predicted surface topography using an Okada [1992] formulation and a combination of grid search and linear least squares inversions. An underlying Okada formulation is used to define the distribution of vertical surface displacement due to 1 m of slip on segment B of the Reelfoot fault (Figure 8). Slip on

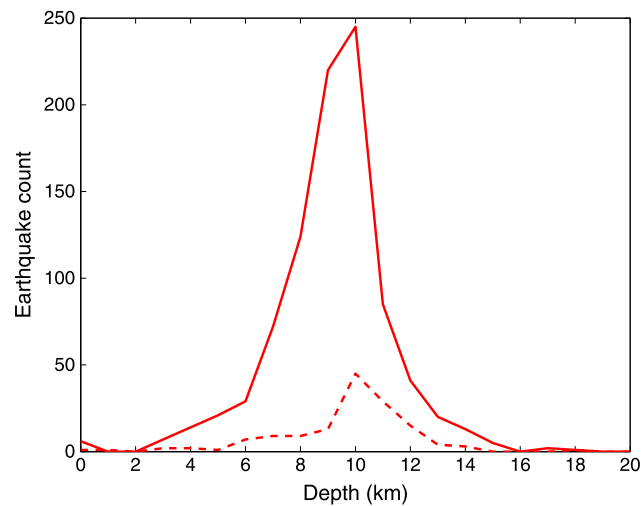


**Figure 9.** Number of relocated earthquakes in 1 km depth bins as a function of depth. The solid line represents earthquake counts summed along the 40 km extent of the Reelfoot fault. The dashed line represents earthquake counts summed along the 20 km extent of the Cottonwood Grove fault.

by about 5% because *Carlson and Guccione* [2010] found that along the Reelfoot scarp, sub-bottom acoustic profiling revealed that structural relief was about 5% greater than the topographic relief. Further, compaction within the hanging wall is not considered, which may lead to an underestimation of total slip.

We assume that the 1812 and 1450 AD Reelfoot events were of similar size and each had an average rupture displacement of 5 m on segment B. This assumption is supported by observations of 1812 and 1450 sand blow fields, which are of similar size [Tuttle *et al.*, 2002], and estimates that uplift along the Reelfoot scarp were less than 5.9–8.2 m in the 1812 event and more than 1.6–3.9 m in the 1450 event [Carlson and Guccione, 2010]. If the magnitude of the December 1811 event on the Cottonwood Grove fault is up to 0.5 units less than the 1812 Reelfoot event [Boyd and Cramer, 2014], displacement in the December event could be more than 75% of that in the February event (Appendix A). We assume that a second 1450 event occurred on the Cottonwood Grove fault and was the same size as the December 1811 event. This assumption is weakly supported by observations of the extent and position of large sand blow fields [Tuttle *et al.*, 2002].

On both the Reelfoot and Cottonwood Grove faults, the downdip extent of coseismic rupture is assumed to lie just below the peak in present-day seismicity or roughly 10 km on average (Figure 9). We assume that this is the transition between predominantly rate-weakening to predominantly rate-strengthening fault friction. The updip limit of rupture on the Reelfoot fault is assumed to reach the surface, whereas for the Cottonwood Grove fault, it is assumed to be 2 km depth. The latter assignment is made because surficial signs of rupture, such as a fault scarp, are not present (though such evidence could have been eroded), and because we assume that events on the Cottonwood Grove fault are smaller than events on the Reelfoot fault. Note, however, that our results are not particularly sensitive to this choice of updip limit of rupture on the Cottonwood Grove fault.

## 5.2. Creep and Regional Strain Models

Multiple models of kinematically prescribed steady creep on dislocations in a half-space are tested using an *Okada* [1992] formulation; models put forth by *Frankel et al.* [2012] and *Pratt* [2012] are considered. In the former, they found that the regional geodetic signal could be explained by creep on a dislocation residing along a downdip extension of the Reelfoot fault between 12 to 20 km depth. In the latter, Pratt suggests that the stepover structure of the NMSZ can be explained by regional shear across a subsurface dislocation oriented N28°E subject to a principal stress oriented N70°E. We consider both simple shear strain and uniaxial compression separately to describe the Pratt model. In addition to creep on these dislocations, creep on a dislocation residing along the downdip extension of the Cottonwood Grove fault is also modeled.

segment A is assumed to be greater by a factor,  $f$ , of  $1/\cos(\phi_U - \phi_L)$  where  $\phi_U$  and  $\phi_L$  are dips of the upper and lower fault segments. This factor is based on conservation of line lengths projected along the dip of the lower fault segment as lower crustal material is thrust up and forced to bend along the shallow fault segment. For a given downdip and updip rupture extent among a grid of potential values, linear least squares is used to solve for a scaling factor (slip) and offset that minimize the difference between observed and predicted vertical surface displacement. We find that the highs in surface topography can be best explained by coseismic and postseismic slip that essentially reaches the surface, extends down to 17 km depth, and has a magnitude of  $9.6 \pm 0.2$  m on segment B. This modeling may underestimate total slip

Surface deformation due to 1 mm/yr of creep on these dislocations is calculated where creep is confined to be dip slip on the downdip extension of the Reelfoot fault and strike slip on the downdip extension of the Cottonwood Grove fault and regional shear dislocation. The dislocations residing along the downdip extensions of the Reelfoot and Cottonwood Grove faults extend from 12 to 20 km depth, lying directly below the more significant concentrations of seismicity and are 40 and 20 km long, respectively. The dislocations have orientations resulting from our analysis of relocated seismicity (Figure 1 and Table 5). The Pratt model shear surface is approximated with a 2000 km long dislocation that extends from 20 to 1000 km depth. A Poisson's ratio of 0.25 is assumed. Uniaxial compression for the Pratt model is implemented by a displacement surface that varies linearly in one direction with a strain of  $1 \times 10^{-9}$  per year. Weighted linear least squares—where the weights are the inverse of the velocity uncertainty—is used to solve for the scaling factor (creep/strain rate) and northerly and easterly translation that minimize the difference between observed and predicted horizontal surface deformation.

### 5.3. Postseismic Models

The program Relax [Barbot *et al.*, 2009] is used to calculate models of viscoelastic relaxation and frictional afterslip from candidate New Madrid earthquakes for various lower crustal/upper mantle viscosities and frictional parameters, respectively. Fault geometry, extent of coseismic rupture, and slip in the 1811–1812 and 1450 events are assumed and detailed in section 5.1. Historic earthquakes on the Reelfoot and Cottonwood Grove faults are confined to be reverse and right lateral, respectively, which is consistent with present-day earthquake focal mechanisms [Johnson *et al.*, 2014]. While some amount of oblique slip could have occurred during the 1811–1812 events, we do not have the information required to constrain these parameters. A grid search is performed to find a lower crustal/upper mantle viscosity and a frictional parameter, respectively, that best fit the observed present-day horizontal surface deformation. The forward model includes estimates of north and east translation components, solved for via weighted least squares where the weights are the inverse of the velocity uncertainty, and these translations are removed prior to evaluating the fit.

The viscoelastic model domain consists of a 20 km thick elastic upper crust on top of a viscoelastic half-space. Viscosities ranging from  $10^{18}$  to  $10^{23}$  Pa s are considered in the grid search. Li *et al.* [2005] evaluated viscosities below 20 km depth ranging from  $10^{19}$  to  $10^{21}$  Pa s. Kenner and Segall [2000] confined their viscoelastic region to a block 5 to 75 km wide by 200 km long at depths between 15 and 40 to 60 km with a viscosity of  $10^{21}$  Pa s. Like these previous authors, a Poisson's ratio of 0.25, shear modulus of 35 GPa, and Young's modulus of 87.5 GPa are assumed. Subsurface rock density is assumed to be  $2700 \text{ kg/m}^3$ .

Frictional afterslip is modeled assuming that afterslip begins immediately below the rupture and is allowed to extend down to 10 times the coseismic fault width and across to five times the coseismic fault length, though most of the afterslip is confined to within several kilometers of the coseismic rupture. These large extents are chosen to minimize edge effects on the afterslip solution. Like the viscoelastic modeling, a half-space with a shear modulus of 35 GPa, Poisson's ratio of 0.25, and density of  $2700 \text{ kg/m}^3$  is assumed.

The program Relax uses a rate-strengthening law on the fault plane accommodating afterslip of the form

$$\dot{s} = 2\dot{s}_0 \sinh \frac{\Delta\tau}{(a-b)\sigma} \quad (3)$$

where  $\dot{s}$  is the slip rate,  $\dot{s}_0$  is a reference slip rate,  $(a - b)$  is a frictional parameter that controls whether the fault is rate strengthening ( $a - b > 0$ ) or rate weakening ( $a - b < 0$ ),  $\Delta\tau$  is the change in shear stress, and  $\sigma$  is the normal stress. This law is a steady state simplification of the more general rate-and-state friction law introduced by others [Lapusta *et al.*, 2000; Rice *et al.*, 2001]. This simplification is achieved by assuming that cumulative afterslip is much greater than the characteristic slip distance, the coseismic stress change is much greater than the background coulomb stress, and the coseismic change in normal stress is negligible compared to background compressive stresses. Barbot *et al.* [2009] found through numerical modeling of GNSS time series during the three years subsequent to the  $M_w 6.0$  2004 Parkfield earthquake that the data could be best explained with the frictional parameter  $(a - b)$  equal to  $7 \times 10^{-3}$  and reference slip rate equal to 20 mm/yr. This value of the frictional parameter is on the high end of laboratory experiments [Marone, 1998], which vary from negative values (velocity weakening) up to 0.006, but because of uncertainties in scaling the laboratory results to the field, we assume the value found by Barbot *et al.* [2009]. We consider a range of

**Table 6.** Modeling Results<sup>a</sup>

Structure	Variable <sup>b</sup>	F-test Prob.	Variance Reduction	$\chi^2$	<i>p</i>
<i>Viscoelastic Response</i>					
Cottonwood Grove fault		47%	0%	19.09	0.4514
Reelfoot fault, seg. B	$0.4 \leq 4.2 \leq 45.0$	51%	5%	17.31	0.5687
<i>Afterslip</i>					
Cottonwood Grove fault		49%	3%	18.81	0.4694
Reelfoot fault, seg. B	$0.05 \leq 0.3 \leq 1.6$	57%	12%	14.64	0.7443
<i>Creeping Dislocations</i>					
Cottonwood Grove fault	$-5.56 \pm 7.87$	44%	-3%	17.06	0.5859
Reelfoot fault	$4.03 \pm 2.31$	67%	22%	10.45	0.9411
Regional shear	$-0.20 \pm 0.27$	47%	2%	57.18	0.0001
<i>Coupled Postseismic Response</i>					
Reelfoot fault, seg. B	$0.03 \leq 7.8 \leq 2200.0$	58%	13%	14.79	0.7353

<sup>a</sup>Positive values of slip rate have right-lateral and thrust sense of movement. Also provided are the associated fitting parameters—variance reduction,  $\chi^2$  statistic, and associated *p*-value, and *F*-test signifying the probability of being better able to predict the observations than would a null hypothesis, a hypothesis in which there is zero ground deformation and observations are the result of random fluctuations.

<sup>b</sup>Variable being solved for viscoelastic response—viscosity ( $10^{21}$  Pa s), afterslip—reference slip rate (mm/yr), creeping dislocation—slip rate (mm/yr), and coupled postseismic response—viscosity ( $10^{21}$  Pa s).

reference slip rate from  $10^{-3}$  to  $10^2$  mm/yr in the grid search, though we note that ground deformation from afterslip several hundred years after the perturbing earthquake will be more strongly sensitive to the ratio of reference slip rate to frictional parameter.

Horizontal stresses are likely to be equal to or larger than vertical stresses at 5–10 km depth in order to explain the distribution of strike-slip and reverse faulting mechanisms [Johnson *et al.*, 2014]. Therefore, at 10 km depth the normal stress on the Reelfoot fault will be at least the lithostatic stress minus the hydrostatic stress or roughly 165 MPa, which results in a value of  $(a - b)\sigma$  of 1.2 MPa.

## 6. Results

The assessment of model results is primarily evaluated with an *F*-test [Menke, 1989], which is the ratio of reduced  $\chi^2$  values for a reference model relative to the model under consideration. For all but the Pratt model in which all 13 geodetic stations are used, there are 22 data points (11 stations each having two components of motion) and three model parameters (offsets in easting and northing and one of reference slip rate or viscosity in the postseismic models, or creep and strain rate in the dislocation and compression models) for the model being tested and two model parameters (offsets in easting and northing) for the reference model. *F*-test probabilities greater than ~0.5 mean that the model under consideration does better than the reference model at reproducing the observations. The reference model is a model in which there is no underlying surface deformation, and data variance is due to inherent randomness. It is equal to the observed data minus the weighted mean of the eastings and northings where the weights are the inverse of the velocity uncertainty. Reported uncertainties in creep are 95% confidence intervals obtained from the diagonal of the model covariance matrix [see Aster *et al.*, 2005, equation (2.30)]. Modeled surface deformation resulting from postseismic processes appears in Figure 5. Modeled surface deformation resulting from kinematically prescribed creep on dislocations within the NMSZ is essentially the same as the dynamic models of afterslip and is not shown. Modeled surface deformation resulting from regional shear and compression has very little deformation within the NMSZ and is not shown.

### 6.1. Individual Dislocation and Postseismic Models

Thrust-sense creep on a dislocation beneath the Reelfoot fault and Reelfoot postseismic frictional afterslip can each yield *F*-test probabilities that suggest that these models have a 67% and 57% probability, respectively, of being better able to predict the observations than the reference model. Variance reductions are 22% and 12%,  $\chi^2$  values are 10 and 15, and associated *p*-values are 0.94 and 0.74 (Table 6). The large *p*-values imply that if these models were the only processes affecting ground deformation, the uncertainties, on average, should be about 20% lower. Our best model of a creeping dislocation has a rate of  $4 \pm 2$  mm/yr,

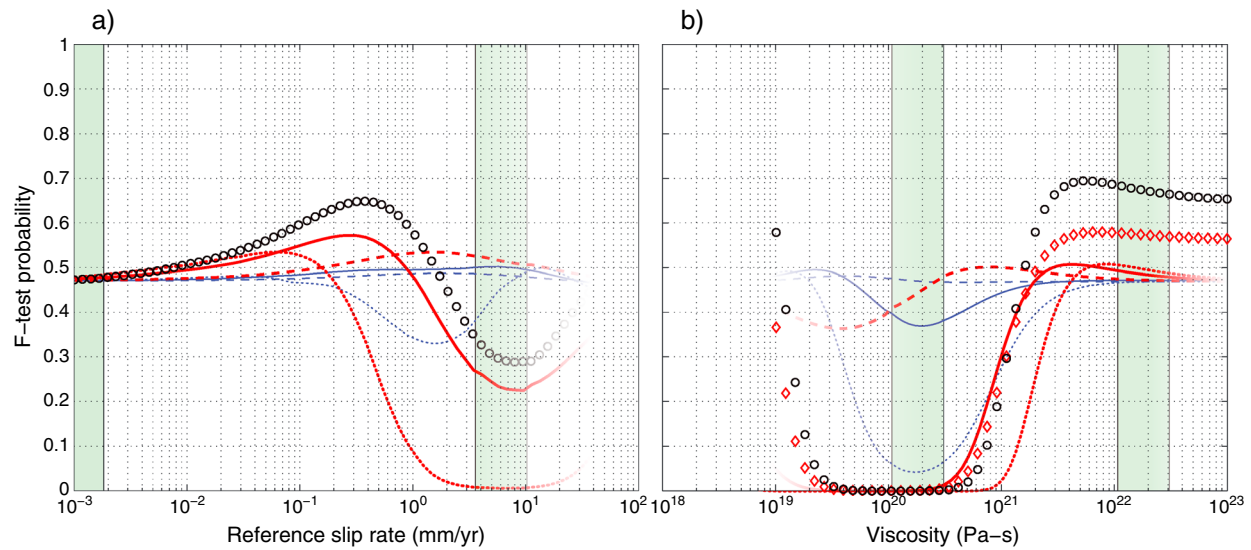


**Figure 10.** *F*-test probability as a function of (a) reference slip rate and (b) viscosity for the Reelfoot fault (thick lines) and Cottonwood Grove fault (thin lines). Solid lines represent models having the slip during rupture reported in Table 5. Dotted lines represent twice that amount of slip and dashed lines, 20%. The areas between vertical bands are regions in which the individual afterslip and viscoelastic modeling results are interpolated to estimate site velocities  $\sim 560$  and  $\sim 200$  years after the 1450 and 1812 events, respectively. Outside these regions, model results are extrapolated and site velocities are less certain. The diamonds represent the coupled afterslip-viscoelastic Reelfoot model with a reference slip rate of 0.3 mm/yr and a depth of rupture of 10 km. No extrapolation was needed to produce the coupled results. The circles represent a depth of rupture on the Reelfoot fault of 12 km and a reference slip rate of 0.4 mm/yr in Figure 10b.

consistent with the results of *Frankel et al.* [2012]. For our modeling of postseismic frictional afterslip, we estimate a reference slip rate of 0.3 mm/yr (Figure 10a). From the curvature of the prediction error at the best fitting reference slip rate [*Aster et al.*, 2005; *Menke*, 1989], 95% confidence limits on this estimate are found to be 0.05 to 1.6 mm/yr.

Models involving the Cottonwood Grove fault—creep on a dislocation beneath the Cottonwood Grove fault and Cottonwood Grove fault postseismic frictional afterslip and viscoelastic relaxation—are not particularly significant with *F*-test probabilities less than 50% and variance reductions of 3% or less.

Models of postseismic viscoelastic relaxation subsequent to ruptures on the Reelfoot fault are marginally significant with an *F*-test probability just greater than 50% and a variance reduction of 5%. For a fault displacement of 5 m in the 1450 and 1812 Reelfoot events, the viscosity that produces the best match to observations is about  $4 \times 10^{21}$  Pa s (Figure 10b). 95% confidence limits on this estimate are between  $4 \times 10^{20}$  and  $4 \times 10^{22}$  Pa s, though these bounds are likely to be shifted to larger values since the prediction error is not symmetric about the best fitting viscosity. Viscosities outside of this range produce a signal that does not match observations and increase the variance of residuals.

The best fitting regional simple shear model yields ground motions that cannot significantly explain the data and suggests that right-lateral creep on the regional dislocation proposed by *Pratt* [2012] is less than 0.1 mm/yr and indistinguishable from 0, which is broadly consistent with the less than 0.2 mm/yr regional slip accrual rate estimated by *Calais and Stein* [2009] and *Craig and Calais* [2014]. Alternatively, if the region can be described by compression with a principle axis oriented N70°E, which was proposed by *Pratt* [2012] as the driving force for shear on a N28°E plane, we find strains of  $-0.9 \times 10^{-9} \pm 1.3 \times 10^{-9}$  per year, again indistinguishable from 0. We take this further by considering compressive strain over a range of angles and find the best least-squares solution for compression to be  $\sim$ N20°E with a rate of  $1\text{--}3 \times 10^{-9}$  per year, though the *F*-test suggests that this solution is not significant. This orientation is consistent with glacial isostatic adjustment [*Calais et al.*, 2006] and the movement of the reference time series but appears incompatible with the more easterly orientation of maximum principal stress derived from earthquake focal mechanisms [*Johnson et al.*, 2014].

## 6.2. Coupled Model on the Reelfoot Fault

Subsequent to rupture, both viscoelastic relaxation and frictional afterslip are likely to take place. We do not test coupled postseismic models from earthquakes on the Cottonwood Grove fault because of the poor

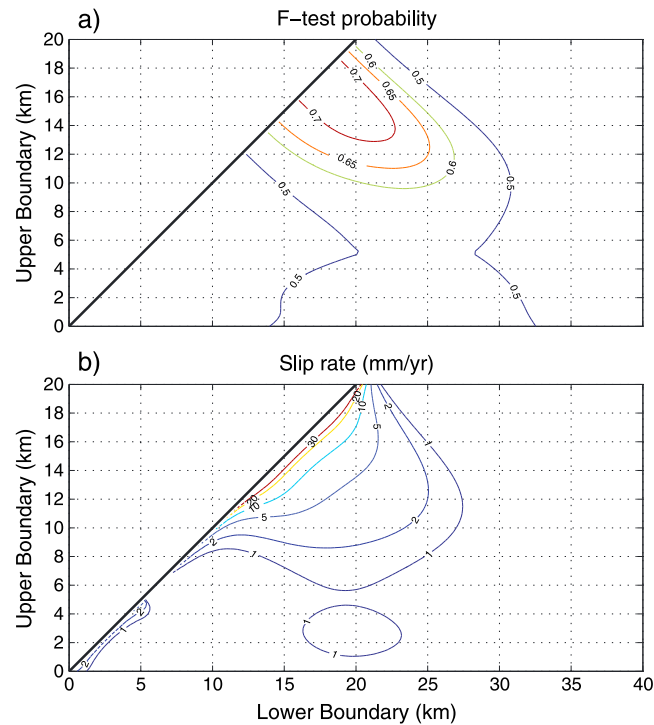


**Figure 11.** Sensitivity of (a) *F*-test probability and (b) slip rate on the updip and downdip depth limits of the creeping dislocation beneath the Reelfoot fault. The heavy diagonal line in each figure represents the limit for which the depth of the lower boundary must be greater than the depth of the upper boundary.

resolution and expected small signal. We test this possibility for the Reelfoot fault and vary viscosity from  $10^{20}$  to  $10^{23}$  Pa s. We define the quantity

$$\psi = \frac{\dot{\epsilon}_0}{(a-b)\sigma}, \quad (4)$$

and hold it constant at 0.25 mm/yr/MPa. The reference slip rate and frictional parameter times fault normal stress are increased by a factor of  $10^3$  in order to make use of the approximation  $\sinh(x) \cong x$  for small  $x$  and be able to generate numerical solutions in a reasonable amount of time. This approximation has a minimal effect on surface velocities several hundred years after the causative event. Its primary effect is to reduce creep on the fault surface close to the earthquake rupture soon after the event. This approximation can be seen as a fault zone width divided by fault zone viscosity, which essentially means that it is not possible to distinguish whether deformation is occurring as afterslip on a discrete fault or as a viscoelastic response distributed over some thin volume about that discrete fault.

Coupling afterslip and viscoelastic relaxation for the 1450 and 1812 earthquakes on the Reelfoot fault yields a large range of *F*-test probabilities greater than 50% for varying viscosity (Figure 10b). The coupled model does poorly for viscosities less than  $2 \times 10^{21}$  Pa s, and the *F*-test probability peaks at 58% for a viscosity of  $8 \times 10^{21}$  Pa s. Above this value, *F*-test probabilities decrease and level off to about 57%. The 95% confidence limits for the best fitting viscosity,  $8 \times 10^{21}$  Pa s, are between  $3 \times 10^{19}$  to  $2 \times 10^{24}$  Pa s. However, like our previous viscoelastic analyses, these bounds are likely to be shifted to larger values because the prediction error is not symmetric about the best fitting viscosity.

## 7. Discussion

### 7.1. Sensitivities

Models of creep on subsurface dislocations have some important sensitivities, the most important of which is the area over which creep occurs. For example, Figure 11 shows the effect of changing the updip and downdip limits of creep on the dislocation beneath the Reelfoot fault. There is a range of updip and downdip limit for which the model produces an acceptable fit. Decreasing the area over which creep can occur increases the amount of creep required to fit the observed surface deformation. But, perhaps of most significance, this analysis suggests that the creeping part of the fault must be relatively shallow (<30 km depth) and lie below the more significant concentrations of present-day seismicity (>10 km depth), in agreement with the analysis of Frankel *et al.* [2012]. The best fit occurs for creep confined to between about 15 and 20 km depth, slightly deeper than presented by Frankel *et al.* [2012].

Regarding dynamic models, care must be taken when interpreting derived values because of uncertainties in various quantities including slip during rupture, subsurface rheology, fault frictional properties, and surface ground deformation, and correlations between different sets of parameters. For example, above about  $10^{21}$  Pa s, the relaxation evolves slowly such that surface deformation is directly proportional to the ratio

of slip during rupture to viscosity; GNSS observations can be fit just as well by increasing the amount of slip during earthquake rupture and increasing the viscosity (Figure 10b). However, below about  $10^{20}$  Pa s, the system evolves quickly, and the relationship between surface deformation, slip during rupture, and viscosity is very different; GNSS observations can be fit just as well by increasing the amount of slip during earthquake rupture and decreasing the viscosity.

Modeling of postseismic frictional afterslip has dependencies similar to modeling of viscoelastic relaxation. Small values of the ratio of reference slip rate to frictional parameter times fault normal stress,  $\psi$ , yield afterslip models that evolve slowly and result in low levels of subsurface creep 200 years after an 1812-type event. In contrast, large values of  $\psi$  yield afterslip models that can evolve very quickly, which, after 200 years, also result in low levels of subsurface creep. Surface motions can be fit (yield positive variance reduction) by increasing slip during rupture and either increasing or decreasing  $\psi$  above or below this transition. As can be seen in Figure 10, we are below this transition as decreasing  $\psi$  requires greater slip to best fit observations.

## 7.2. Causes of Creep

While a model of creep on a dislocation residing along the downdip extension of the Reelfoot fault can reproduce much of the signal in the GNSS motions, the model is kinematic and requires a driving mechanism. Because the signal is local, so too is likely the cause; postseismic frictional afterslip from the February 1812 earthquake is a natural explanation. Mechanisms in which a frictional dislocation is embedded within broad scale deformation resulting from stresses imposed at the sides of the north American plate or from below [Forte *et al.*, 2007] or from glacial isostatic adjustment [Sella *et al.*, 2007] do not appear to fully explain this creeping model as we would have to see far more significant far-field deformation, larger than what we infer on the dislocation (4 mm/yr). Across the region, stations are approaching each other on average at rates of less than 0.2 mm/yr [Craig and Calais, 2014]. A more local signal could be generated by erosion of the Mississippi River valley [Calais *et al.*, 2010], but with only 12 m of erosion between 16 and 10 kyr BP, present-day creep from something like afterslip on the downdip extension of the Reelfoot fault should be far less than 1.5 mm/yr. One could potentially appeal to time-variable creep to reconcile the localized signal and relatively small regional motions and speculate that the present-day creep on the Reelfoot fault is a “slow slip” event [Schwartz and Rokosky, 2007], but additional research is required to test this type of possibility. In any case, we expect that these other sources of stress do contribute to surface deformation, the long-term build up of stress, and the triggering of earthquake sequences.

Frankel *et al.* [2012] argue that the creep on the Reelfoot fault cannot be postseismic frictional afterslip because if it were, they would also infer creep on the Cottonwood Grove fault evidenced by northward motion of station *ptgv* relative to *stle*, which they do not see. Given the uncertainties in station velocities, we do not think that this conclusion can be made with a single pair of stations. However, when considering all stations in the area, we are not able to fit the data with creep or postseismic models on the Cottonwood Grove fault. But this does not necessarily mean that these deformation mechanisms are not present. Part of the reason that these mechanisms are not as well fit as on the Reelfoot fault may be because (1) the magnitude of the 1811 earthquake on the Cottonwood Grove fault may be up to 0.5 magnitude units smaller than the 1812 Reelfoot event [Bakun and Hopper, 2004; Boyd and Cramer, 2014; Cramer and Boyd, 2014; Hough *et al.*, 2000], and hence, the amount and extent of afterslip and viscoelastic relaxation would also be smaller; and (2) the GNSS stations are not as well positioned to see creep or afterslip on the Cottonwood Grove fault (Figure 5).

Our model of postseismic frictional afterslip does not match the observations as well as the creep model. This is due to the depth at which much of the afterslip in our model takes place, between about 10 and 15 km depth. We see from Figure 11 that at this depth, *F*-test probabilities for a creep model are just over 50%. It is possible that coseismic rupture extended into the rate-strengthening region of the fault, deepening the afterslip response. If we consider uniform coseismic rupture extending to 12 km depth rather than 10, the peak in *F*-test probabilities increases from 57% to 65% and the reference slip rate increases to 0.4 mm/yr (Figure 10a). Reconsidering the coupled afterslip-viscoelastic Reelfoot model, we find that the peak in *F*-test probabilities increases from 58% to 70% (Figure 10b). This modeling could be further refined to improve the fit to observations by considering nonuniform rupture and depth-dependent frictional properties, but the substantial observational uncertainty and limited number of GNSS sites make this additional analysis poorly constrained. We advocate for additional high quality recording sites in operation for at least 10 years [see, e.g., Boyd *et al.*, 2013; Hamburger *et al.*, 2014].

### 7.3. Fault Friction

While postseismic frictional afterslip is proposed as an explanation for creep, it is difficult to precisely constrain how deformation is occurring or what the frictional parameters might be. As noted in section 6.2, after several hundred years following an earthquake, it may not be possible to distinguish afterslip from a viscoelastic response occurring over some thin volume of material about the fault. If the cause of the creep signal is afterslip, for small ratios of  $\Delta\tau / (a - b)\sigma$ , the afterslip response is directly proportional to  $\psi$ , the ratio of reference slip rate to frictional parameter times fault normal stress;  $\dot{s} = 2\dot{s}_0 \sinh[\Delta\tau / (a - b)\sigma] \cong 2\psi\Delta\tau$  for small  $\Delta\tau / (a - b)\sigma$ . So in the case of  $(a - b)\sigma$  equal to 1.2 MPa and coseismic rupture extending to 12 km depth, the greatest  $F$ -test probability occurs for a value of  $\dot{s}_0$  of about 0.4 mm/yr. For comparison, the ratio of reference slip rate to frictional parameter found by *Barbot et al.* [2009] for frictional afterslip on the Parkfield segment of the San Andreas fault is over 50 times greater than that found here. To obtain the same quality of fit with a greater amount of slip during rupture would require that  $\psi$  decrease further (Figure 10a). This observation of a relatively low ratio of reference slip rate to frictional parameter seems reasonable for an intraplate fault that is being stressed more slowly than a fault along a plate boundary.

### 7.4. Lower Crustal Viscosity

Modeling coupled frictional afterslip-viscoelastic mechanisms for the February 1812 Reelfoot event can help constrain lower crustal viscosity. This modeling suggests that lower crustal viscosity is greater than about  $1.5 \times 10^{21}$  Pa s (Figure 10b). Values lower than this significantly degrade the fit between observed and modeled surface displacements, whereas values above  $\sim 5 \times 10^{21}$  Pa s yield a relatively large and constant  $F$ -test probability. For coseismic rupture extending to 12 km depth,  $F$ -test probabilities remain above 65% with a peak of 70% at  $5 \times 10^{21}$  Pa s.

Studies of post-glacial rebound are commonly used to infer mantle viscosity structure but are insensitive to viscosity structure below about 1800 km depth and cannot distinguish a detailed profile above [*Paulson et al.*, 2007]. Under the assumption of a homogeneous mantle, *Paulson et al.* [2007] find viscosities below North America that range from  $1.4 \times 10^{21}$  to  $2.3 \times 10^{21}$  Pa s. If a two-layer model is adopted, split at 670 km depth, mantle viscosities for the upper and lower mantle are  $5 \times 10^{20}$  and  $2.3 \times 10^{21}$  Pa s, respectively. In several studies of viscoelastic relaxation following the 1959 Hebgen Lake earthquake [*Chang et al.*, 2013; *Hammond et al.*, 2009; *Nishimura and Thatcher*, 2003, 2004], lower crustal viscosities in the vicinity of the Hebgen Lake fault are estimated to range from  $3 \times 10^{20}$  to  $3 \times 10^{21}$  Pa s. Taken together, these other studies suggest that the value of  $\sim 5 \times 10^{21}$  Pa s estimated in this paper for the lower crust/upper mantle beneath the NMSZ seems reasonable.

### 7.5. Aftershocks

If the relatively shallow creep is frictional afterslip, it may mean that much of the seismicity in the region represent aftershocks of the 1811–1812 events [*Stein and Liu*, 2009]. Many studies have argued in favor of a relation between aftershocks and postseismic afterslip [*Barbot et al.*, 2009; *Hsu et al.*, 2006; *Perfettini and Avouac*, 2004, 2007]. In the Stable Continental Region of North America, there have been studies arguing for [*Ma and Eaton*, 2007; *Stein and Liu*, 2009] and against [*Ebel*, 2009; *Fereidoni and Atkinson*, 2014; *Page and Hough*, 2014] long-lived aftershock sequences. We expect that the spatial and temporal extent of an aftershock sequence will depend on the size and location of the main shock and the rheology of the surrounding material.

With regard to aftershocks of the 1811–1812 events, *Page and Hough* [2014] argue based on Epidemic Type Aftershock Sequence (ETAS) modeling that the low rate of M6 and greater earthquakes since 1813 implies that it is unlikely that the high recent rate of M4 and greater earthquakes in the NMSZ represent aftershocks of the 1811–1812 main shocks. In ETAS [*Ogata*, 1988], the rate of aftershocks,  $R(t)$ , as a function of time,  $t$ , resulting from a main shock,  $M$ , greater than a given magnitude,  $M_{\min}$ , is based on the modified Omori law [*Utsu*, 1961] and given by

$$R(t) = \frac{10^{a+b(M-M_{\min})}}{(c+t)^p} \quad (5)$$

where  $a$ ,  $b$ ,  $c$ , and  $p$  are constants. *Page and Hough* derive a value for  $b$  from central U.S. earthquake catalogs and solve for the best fitting values of  $a$  and  $p$ . They assume  $c = 0.095$ , which was derived for California

catalogs [Felzer *et al.*, 2003]. Dieterich [1994] argued that rate-and-state friction yields a form similar to the Omori law where

$$c = t_a \left( \frac{r}{R_0} \right), \quad (6)$$

Here  $t_a$  is aftershock duration,  $r$  is the reference earthquake rate, and  $R_0$  is the earthquake rate immediately following the earthquake. The aftershock duration is equal to

$$t_a = \frac{(a - b)\sigma}{\dot{\tau}} \quad (7)$$

where  $\dot{\tau}$  is the background stressing rate.

Equation (7) has a form similar to the inverse of  $\psi$ , which, in this study, is estimated to be over a factor of 50 larger than what was derived for postseismic frictional afterslip from the Parkfield earthquake. If  $1/c$  is proportional to background stressing rate or reference slip rate, for which it is reasonable to consider that both may be smaller in intraplate settings,  $c$  may be far larger for the New Madrid seismic zone than was assumed in the Page and Hough [2014] study. Increasing the value of  $c$  in their analysis would help to resolve the discrepancy they observe between the older rate of M6 and relatively large recent rate of M4 and greater earthquakes.

## 8. Conclusions

GNSS data in and around the New Madrid seismic zone has been reanalyzed, and several deformation models are found to be consistent with surface observations. The results of Frankel *et al.* [2012] are confirmed in that a dislocation creeping at about 4 mm/yr below the Reelfoot fault can reasonably reproduce the GNSS observations. Further, the present study finds that this creep can result from postseismic frictional afterslip from the 1450 AD and February 1812 earthquakes on the Reelfoot fault. Viscoelastic relaxation from events on the Reelfoot fault as well as afterslip from events on the Cottonwood Grove fault have some marginal power to help explain the observations given the expected sense and magnitude of rupture. Following the model proposed by Pratt [2012] in which the structure of the New Madrid seismic zone results from right-lateral slip on a deeply buried northeast trending regional shear surface, we find that slip on this structure is less than 0.2 mm/yr and indistinguishable from 0.0, consistent with the results of Calais and Stein [2009] and Craig and Calais [2014]. Further, if the region can be described by compression with a principle axis oriented N70°E, we find strains of  $0.5 \times 10^{-9} \pm 1.3 \times 10^{-9}$  per year, again indistinguishable from 0.

Modeling afterslip from events on the Reelfoot fault suggests that the ratio of reference slip rate to the product of frictional parameter ( $a - b$ ) and fault normal stress is on the order of 0.3 mm/yr/MPa or about 50 times smaller than that derived for the Parkfield segment of the San Andreas fault. Modeling both afterslip and viscoelastic relaxation postseismic processes from the 1450 and 1812 Reelfoot fault earthquakes leads to the conclusion that lower crustal/upper mantle viscosities are at least  $10^{21}$  Pa s and may be about  $5 \times 10^{21}$  Pa s.

If the GNSS observations reflect afterslip from the 1811–1812 events, it means that much of the seismic activity in the region may represent a long-lived aftershock sequence. But this does not mean that the New Madrid seismic zone will not continue to produce damaging earthquakes or major New Madrid 1811–1812-type earthquakes over relatively short recurrence intervals (~500 years). Earthquake clustering has been observed for intraplate settings [Crone *et al.*, 1997], and this idea and our results are consistent with the modeling results of Kenner and Segall [2000] who propose that sequences of M7+ earthquakes can cluster over short recurrence intervals due to reloading from postseismic processes.

## Appendix A: Earthquake Magnitude and Relative Displacement

An estimate of the moment magnitude of the 1812 Reelfoot event can be made with the rupture parameters in this study. Seismic moment is given by

$$M_0 = \mu \Omega D \quad (A1)$$

where  $\mu$  is the shear modulus,  $\Omega$  is the area (length,  $L$ , times width,  $W$ ) of the fault surface, and  $D$  is the average displacement on the fault [Aki, 1966]. The total seismic moment is  $1.0 \times 10^{20}$  Nm for a fault area of  $40 \times 5.2$  km<sup>2</sup>, average displacement of 6.6 m, and shear modulus of 25 GPa on the shallow segment, segment A, and fault area of  $40 \times 9.2$  km<sup>2</sup>, an average displacement of 5.0 m, and a shear modulus of 35 GPa on the

deeper segment, segment B. Using the relation of *Hanks and Kanamori* [1979], this yields a moment magnitude of 7.3. Their equation relating seismic moment and moment magnitude, however, assumes a constant ratio of stress drop,  $\Delta\phi$ , to shear modulus,  $\mu$ , equal to  $1 \times 10^{-4}$ . If this assumption is relaxed, moment magnitude is given by

$$M_W = \frac{2}{3} \log_{10} \left( \frac{\Delta\phi}{2\mu} M_0 \right) - 3.2 \quad (\text{A2})$$

where the variables are in the International System of Units. If the average stress drop for a thrust earthquake in which the upper edge is relaxed (lower Reelfoot fault segment, as indicated by subscript  $\text{L}$ ) can be approximated by

$$\Delta\phi_{\text{L}} \approx \frac{\mu_{\text{L}} D_{\text{L}}}{2W_{\text{L}}}, \quad (\text{A3})$$

and both upper and lower edges are relaxed (upper Reelfoot fault segment, as indicated by subscript  $\text{U}$ ),

$$\Delta\phi_{\text{U}} \approx \frac{\mu_{\text{U}} D_{\text{U}}}{L_{\text{U}}}, \quad (\text{A4})$$

the moment magnitude for the 1812 event is 7.5, which is consistent with recent estimates near 7.5 using felt intensities [Boyd and Cramer, 2014; Cramer and Boyd, 2014]. Notice that this formulation is independent of downdip rupture width on the deeper segment because seismic moment is a function of downdip width, and stress drop is an inverse function of downdip width. However, if the rupture length is increased by 20 km, the magnitude estimate will increase to 7.6.

If the difference in magnitude between the December 1811 and February 1812 events is up to 0.5 units [Boyd and Cramer, 2014], this suggests that displacement in the December event could be more than 75% of that in the February event,

$$\frac{D_{\text{C}}}{D_{\text{L}}} = \left[ \left( \frac{L_{\text{L}}}{2W_{\text{C}}} + \frac{\mu_{\text{U}} f W_{\text{U}}}{2\mu_{\text{L}} W_{\text{C}}} \right) 10^{\frac{3}{2}(M_{\text{WC}} - M_{\text{WR}})} \right]^{\frac{1}{2}} \approx 0.75,$$

where stress drop in the December event is assumed to be  $\mu D/L$  and the subscripts  $\text{C}$  and  $\text{R}$  refer to the Cottonwood Grove and Reelfoot events, respectively.

#### Acknowledgments

The GNSS data analyzed in this paper were obtained from the USGS website <http://earthquake.usgs.gov/monitoring/gps/CentralUS/> in January 2014. Duncan Agnew is gratefully acknowledged for providing routines to calculate flicker noise in GNSS time series. Sylvain Barbot provided important feedback on the use of the program Relax. Eric Jones provided high resolution topographic data of the New Madrid seismic zone. Paul Segall, Michael Hamburger, John Langbein, Fred Pollitz, and Rob Williams provided thorough reviews that helped improve the clarity and significance of this manuscript. Any use of trade, product, or firm names is for descriptive purposes only and does not imply endorsement by the U.S. Government.

#### References

- Aki, K. (1966), Generation and propagation of G waves from the Niigata earthquake of June 16, 1964. Part 2. Estimation of earthquake moment, released energy, and stress-strain drop from the G wave spectrum, *Bull. Earthquake Res. Inst.*, *44*, 73–88.
- Altamimi, Z., X. Collilieux, and L. Metivier (2011), ITRF2008: An improved solution of the international terrestrial reference frame, *J. Geod.*, *85*(8), 457–473.
- Aster, R. C., B. Borchers, and C. H. Thurber (2005), *Parameter Estimation and Inverse Problems*, 301 pp., Elsevier, San Diego, Calif.
- Bakun, W. H., and M. G. Hopper (2004), Magnitudes and locations of the 1811–1812 New Madrid, Missouri, and the 1886 Charleston, South Carolina, earthquakes, *Bull. Seismol. Soc. Am.*, *94*(1), 64–75.
- Barbot, S., Y. Fialko, and Y. Bock (2009), Postseismic deformation due to the Mw 6.0 2004 Parkfield earthquake: Stress driven creep on a fault with spatially variable rate-and-state friction parameters, *J. Geophys. Res.*, *114*, B07405, doi:10.1029/2008JB005748.
- Bertiger, W., S. D. Desai, B. Haines, N. Harvey, A. W. Moore, S. Owen, and J. P. Weiss (2010), Single receiver phase ambiguity resolution with GPS data, *J. Geod.*, *84*(5), 327–337.
- Boyd, O. S., and C. H. Cramer (2014), Estimating earthquake magnitudes from reported intensities in the central and eastern United States, *Bull. Seismol. Soc. Am.*, *104*(4), 1709–1722.
- Boyd, O. S., E. Calais, J. Langbein, H. Magistrale, S. Stein, and M. D. Zoback (2013), Workshop on New Madrid geodesy and the challenges of understanding intraplate earthquakes, *U.S. Geol. Surv. Open File Rep.*, *2013–1004*, p. 35.
- Calais, E., and S. Stein (2009), Time-variable deformation in the New Madrid seismic zone, *Science*, *323*(5920), 1442–1442, doi:10.1126/science.1168122.
- Calais, E., J. Y. Han, C. DeMets, and J. M. Nocquet (2006), Deformation of the North American plate interior from a decade of continuous GPS measurements, *J. Geophys. Res.*, *111*, B06402, doi:10.1029/2005JB004253.
- Calais, E., A. M. Freed, R. V. Arsdale, and S. Stein (2010), Triggering of New Madrid seismicity by late-Pleistocene erosion, *Nature*, *466*, 608–611.
- Cane, M. A., and S. E. Zebiak (1985), A theory for El-Nino and the Southern Oscillation, *Science*, *228*(4703), 1085–1087.
- Carlson, S. D., and M. J. Guccione (2010), Short-term uplift rates and surface deformation along the Reelfoot Fault, New Madrid Seismic Zone, *Bull. Seismol. Soc. Am.*, *100*(4), 1659–1677, doi:10.1785/0120100069.
- Chang, W. L., R. B. Smith, and C. M. Puskas (2013), Effects of lithospheric viscoelastic relaxation on the contemporary deformation following the 1959 Mw 7.3 Hebgen Lake, Montana, earthquake and other areas of the intermountain seismic belt, *Geochem. Geophys. Geosyst.*, *14*, 1–17, doi:10.1029/2012GC004424.
- Craig, T. J., and E. Calais (2014), Strain accumulation in the New Madrid and Wabash Valley seismic zones from 14 years of continuous GPS observation, *J. Geophys. Res. Solid Earth*, *119*, 9110–9129, doi:10.1002/2014JB011498.
- Cramer, C. H., and O. S. Boyd (2014), Why the New Madrid earthquakes are M7–8 and the Charleston earthquake is ~M7, *Bull. Seismol. Soc. Am.*, *104*, 2884–2903, doi:10.1785/0120120257.

- Crone, A. J., M. N. Machette, and J. R. Bowman (1997), Episodic nature of earthquake activity in stable continental regions revealed by palaeoseismicity studies of Australian and North American quaternary faults, *Aust. J. Earth Sci.*, *44*(2), doi:10.1080/08120099708728304.
- DeShon, H. R., S. T. Bisrat, and C. A. Powell (2011), Characterizing complex faulting and near fault velocity and attenuation heterogeneity along the New Madrid Seismic Zone Abstract S11B-2227 presented at 2011 Fall Meeting, AGU, San Francisco, Calif., 5–9 Dec.
- Dieterich, J. (1994), A constitutive law for rate of earthquake production and its application to earthquake clustering, *J. Geophys. Res.*, *99*(B2), 2601–2618, doi:10.1029/93JB02581.
- Dunn, M., H. R. DeShon, and C. A. Powell (2013), Imaging the New Madrid Seismic Zone using double-difference tomography, *J. Geophys. Res. Solid Earth*, *118*, 5404–5416, doi:10.1002/jgrb.50384.
- Ebel, J. (2009), Analysis of aftershock and foreshock activity in stable continental regions: Implications for aftershock forecasting and the hazard of strong earthquakes, *Seismol. Res. Lett.*, *80*(6), 1062–1068, doi:10.1785/gssrl.80.6.1062.
- Enfield, D. B., A. M. Mestas-Nunez, and P. J. Trimble (2001), The Atlantic multidecadal oscillation and its relation to rainfall and river flows in the continental US, *Geophys. Res. Lett.*, *28*(10), 2077–2080, doi:10.1029/2000GL012745.
- Felzer, K. R., R. E. Abercrombie, and G. Ekström (2003), Secondary aftershocks and their importance for aftershock forecasting, *Bull. Seismol. Soc. Am.*, *93*, 1433–1448.
- Fereidoni, A., and G. M. Atkinson (2014), Aftershock statistics for earthquakes in the St. Lawrence Valley, *Seismol. Res. Lett.*, *85*(5), 1125–1136, doi:10.1785/0220140042.
- Forste, A. M., J. X. Mitrovica, R. Moucha, N. A. Simmons, and S. P. Grand (2007), Descent of the ancient Farallon slab drives localized mantle flow below the New Madrid seismic zone, *Geophys. Res. Lett.*, *34*, L04308, doi:10.1029/2006GL027895.
- Frankel, A., R. Smalley, and J. Paul (2012), Significant motions between GPS sites in the New Madrid region: Implications for seismic hazard, *Bull. Seismol. Soc. Am.*, *102*(2), 479–489.
- Gershunov, A., and T. P. Barnett (1998), Interdecadal modulation of ENSO teleconnections, *Bull. Am. Meteorol. Soc.*, *79*(12), 2715–2725.
- Gesch, D., M. Oimoen, S. Greenlee, C. Nelson, M. Steuck, and D. Tyler (2002), The National Elevation Dataset, *Photogramm. Eng. Remote Sens.*, *68*(1), 5–11.
- Hamburger, M. W., O. S. Boyd, E. Calais, N. E. King, and S. A. Stein (2014), Advancing geodesy in the U.S. Midcontinent: Workshop report, *U.S. Geol. Surv. Open File Rep.*, 2014–1169, p. 22.
- Hammond, W. C., C. Kreemer, and G. Blewitt (2009), Geodetic constraints on contemporary deformation in the northern Walker Lane: 3. Postseismic relaxation in the Central Nevada Seismic Belt, in *Late Cenozoic Structure and Evolution of the Great Basin–Sierra Nevada Transition*, edited by J. S. Oldow and P. Cashman, *Geol. Soc. of Am. Spec. Pap.*, pp. 33–54, doi:10.1130/2009.2447(03).
- Hanks, T. C., and H. Kanamori (1979), A moment magnitude scale, *J. Geophys. Res.*, *84*(B5), 2348–2350, doi:10.1029/JB084iB05p02348.
- Hildenbrand, T. G., and J. D. Hendricks (1995), Geophysical setting of the Reelfoot Rift and relations between rift structures and the New Madrid seismic zone, *U.S. Geol. Surv. Prof. Pap.*, 1538-E, 1–30.
- Hough, S. E., and M. Page (2011), Towards a consistent model for strain accrual and release for the New Madrid seismic zone, central United States, *J. Geophys. Res.*, *116*, B03311, doi:10.1029/2010JB007783.
- Hough, S. E., J. G. Armbruster, L. Seeber, and J. F. Hough (2000), On the modified Mercalli intensities and magnitudes of the 1811–1812 New Madrid earthquakes, *J. Geophys. Res.*, *105*(B10), 23,839–23,864, doi:10.1029/2000JB900110.
- Hough, S. E., R. Bilham, K. Mueller, W. Stephenson, R. Williams, and J. Odum (2005), Wagon loads of sand blows in White County, Illinois, *Seismol. Res. Lett.*, *76*, 373–386.
- Hsu, Y.-J., M. Simons, J.-P. Avouac, J. Galetzka, K. Sieh, M. Chlieh, D. Natawidjaja, L. Prawirodirdjo, and Y. Bock (2006), Frictional afterslip following the 2005 Nias-Simeulue earthquake, Sumatra, *Science*, *312*, 1921–1926.
- Johnson, G. A., S. P. Horton, M. Withers, and R. Cox (2014), Earthquake focal mechanisms in the New Madrid seismic zone, *Seis. Res. Lett.*, *85*(2), 257–267.
- Johnston, A. C. (1996), Seismic moment assessment of earthquakes in stable continental regions, III. New Madrid 1811–1812, Charleston 1886, and Lisbon 1755, *Geophys. J. Int.*, *126*(2), 314–344.
- Johnston, A. C., and E. S. Schweig (1996), The enigma of the New Madrid earthquakes of 1811–1812, *Annu. Rev. Earth Planet. Sci.*, *24*, 339–384.
- Kenner, S. J., and P. Segall (2000), A mechanical model for intraplate earthquakes: Application to the New Madrid seismic zone, *Science*, *289*, 2329–2332.
- Langbein, J. (2004), Noise in two-color electronic distance meter measurements revisited, *J. Geophys. Res.*, *109*, B04406, doi:10.1029/2003JB002819.
- Lapusta, N., J. R. Rice, Y. Ben-Zion, and G. Zheng (2000), Elastodynamic analysis for slow tectonic loading with spontaneous rupture episodes on faults with rate- and state-dependent friction, *J. Geophys. Res.*, *105*, 23,765–23,789, doi:10.1029/2000JB900250.
- Li, Q., M. Liu, and E. Sandvol (2005), Stress evolution following the 1811–1812 large earthquakes in the New Madrid Seismic Zone, *Geophys. Res. Lett.*, *32*, L11310, doi:10.1029/2004GL022133.
- Ma, S., and D. W. Eaton (2007), Western Quebec seismic zone (Canada): Clustered, midcrustal seismicity along a Mesozoic hot spot track, *J. Geophys. Res.*, *112*, B06305, doi:10.1029/2006JB004827.
- Mao, A., C. A. Harrison, and T. Dixon (1999), Noise in GPS coordinate time series, *J. Geophys. Res.*, *104*(B2), 2797–2816, doi:10.1029/1998JB900033.
- Marone, C. J. (1998), Laboratory-derived friction laws and their application to seismic faulting, *Annu. Rev. Earth Planet. Sci.*, *26*, 643–696, doi:10.1146/annurev.earth.26.1.643.
- Menke, W. (1989), *Geophysical Data Analysis: Discrete Inverse Theory*, Academic Press, San Diego, Calif.
- Mo, K. C. (2010), Interdecadal modulation of the impact of ENSO on precipitation and temperature over the United States, *J. Clim.*, *23*(13), 3639–3656.
- Mueller, K., and J. Pujol (2001), Three-dimensional geometry of the Reelfoot blind thrust: Implications for moment release and earthquake magnitude in the New Madrid seismic zone, *Bull. Seismol. Soc. Am.*, *91*, 1563–1573.
- Nishimura, T., and W. Thatcher (2003), Rheology of the lithosphere inferred from postseismic uplift following the 1959 Hebgen Lake earthquake, *J. Geophys. Res.*, *108*(B8), 2389, doi:10.1029/2002JB002191.
- Nishimura, T., and W. Thatcher (2004), Correction to “Rheology of the lithosphere inferred from postseismic uplift following the 1959 Hebgen Lake earthquake”, *J. Geophys. Res.*, *109*, B02311, doi:10.1029/2003JB002798.
- Ogata, Y. (1988), Statistical models for earthquake occurrences and residual analysis for point processes, *J. Am. Stat. Assoc.*, *83*, 9–27, doi:10.1080/01621459.1988.10478560.
- Okada, Y. (1992), Internal deformation due to shear and tensile faults in a half-space, *Bull. Seismol. Soc. Am.*, *82*, 1018–1040.
- Page, M., and S. Hough (2014), The New Madrid Seismic Zone: Not dead yet, *Science*, *343*(6172), 762–764.
- Paulson, A., S. Zhong, and J. Wahr (2007), Inference of mantle viscosity from GRACE and relative sea level data, *Geophys. J. Int.*, *171*, 497–508, doi:10.1111/j.1365-246X.2007.03556.x.

- Perfettini, H., and J.-P. Avouac (2004), Postseismic relaxation driven by brittle creep: A possible mechanism to reconcile geodetic measurements and the decay rate of aftershocks, application to the Chi-Chi earthquake, Taiwan, *J. Geophys. Res.*, *109*, B02304, doi:10.1029/2003JB002488.
- Perfettini, H., and J.-P. Avouac (2007), Modeling afterslip and aftershocks following the 1992 Landers earthquake, *J. Geophys. Res.*, *112*, B07409, doi:10.1029/2006JB004399.
- Pollitz, F. F., L. Kellogg, and R. Burgmann (2001), Sinking mafic body in a reactivated lower crust: A mechanism for stress concentration at the New Madrid Seismic Zone, *Bull. Seismol. Soc. Am.*, *91*(6), 1882–1897.
- Pratt, T. L. (2012), Kinematics of the New Madrid seismic zone, central United States, based on stepover models, *Geology*, *40*, 371–374, doi:10.1130/G32624.1.
- Rice, J. R., N. Lapusta, and K. Ranjith (2001), Rate and state dependent friction and the stability of sliding between elastically deformable solids, *J. Mech. Phys. Solids*, *49*, 1865–1898, doi:10.1016/S0022-5096(01)00042-4.
- Roeloffs, E. A. (2001), Creep rate changes at Parkfield, California 1966–1999: Seasonal, precipitation induced, and tectonic, *J. Geophys. Res.*, *106*(B8), 16,525–16,547, doi:10.1029/2001JB000352.
- Schwartz, S. Y., and J. M. Rokosky (2007), Slow slip events and seismic tremor at circum-Pacific subduction zones, *Rev. Geophys.*, *45*, RG3004, doi:10.1029/2006RG000208.
- Sella, G. F., S. Stein, T. H. Dixon, M. Craymer, T. S. James, S. Mazzotti, and R. K. Dokka (2007), Observation of glacial isostatic adjustment in “stable” North America with GPS, *Geophys. Res. Lett.*, *34*, L02306, doi:10.1029/2006GL027081.
- Silverii, F., N. D’Agostino, and M. Metois (2014), Postseismic viscoelastic relaxation following the L’Aquila 2009 earthquake: Implications for lithospheric rheology of the Apennines, Abstract T41C-4629 presented at 2014 Fall Meeting, AGU, San Francisco, Calif., 15–19 Dec.
- Stein, S., and M. Liu (2009), Long aftershock sequences within continents and implications for earthquake hazard assessment, *Nature*, *462*, 87–89.
- Swindel, B. F. (1976), Good ridge estimators based on prior information, *Commun. Stat.-Theory Methods*, *5*, 1065–1075, doi:10.1080/03610927608827423.
- Thomson, D. J. (1982), Spectrum estimation and harmonic analysis, *Proc. IEEE*, *70*, 1055–1096.
- Tuttle, M. P., E. S. Schweig, J. D. Sims, R. H. Lafferty, L. W. Wolf, and M. L. Haynes (2002), The earthquake potential of the New Madrid seismic zone, *Bull. Seismol. Soc. Am.*, *92*(6), 2080–2089.
- Tuttle, M. P., E. S. Schweig, J. Campbell, P. M. Thomas, J. D. Sims, and R. H. I. Lafferty (2005), Evidence for New Madrid earthquakes in A.D. 300 and 2340 B.C., *Seismol. Res. Lett.*, *76*, 489–501.
- Utsu, T. (1961), A statistical study on the occurrence of aftershocks, *Geophys. Mag.*, *30*, 521–605.
- Van Arsdale, R., J. Purser, W. Stephenson, and J. Odum (1998), Faulting along the Southern Margin of Reelfoot Lake, Tennessee, *Bull. Seismol. Soc. Am.*, *88*, 131–139.
- Wdowinski, S., Y. Bock, J. Zhang, P. Fang, and J. Genrich (1997), Southern California permanent GPS geodetic array: Spatial filtering of daily positions for estimating coseismic and postseismic displacements induced by the 1992 Landers earthquake, *J. Geophys. Res.*, *102*(B8), 18,057–18,070, doi:10.1029/97JB01378.
- Williams, S. D. P. (2003), The effect of colored noise on the uncertainties of rates estimated from geodetic time series, *J. Geod.*, *76*, 483–494.
- Zhang, J., Y. Bock, H. Johnson, P. Fang, W. Simon, J. Genrich, S. Wdowinski, and J. Behr (1997), Southern California permanent GPS geodetic array: Error analysis of daily position estimates and site velocities, *J. Geophys. Res.*, *102*(B8), 18,035–18,055, doi:10.1029/97JB01380.
- Zumberge, J. F., M. B. Heflin, D. C. Jefferson, M. M. Watkins, and F. H. Webb (1997), Precise point positioning for the efficient and robust analysis of GPS data from large networks, *J. Geophys. Res.*, *102*(B3), 5005–5017, doi:10.1029/96JB03860.